

# Lawrence Berkeley National Laboratory

## Lawrence Berkeley National Laboratory

**Title**

THE THERMAL EXPANSION OF THE DIRECTIONALLY SOLIDIFIED Al-CuAl<sub>2</sub> EUTECTIC

**Permalink**

<https://escholarship.org/uc/item/0634502p>

**Author**

Baker, Dennis Frank

**Publication Date**

1978-06-01

LBL-7682

C.2

THE THERMAL EXPANSION OF THE DIRECTIONALLY  
SOLIDIFIED Al-CuAl<sub>2</sub> EUTECTIC

Dennis Frank Baker  
(M. S. thesis)

RECEIVED  
LAWRENCE  
BERKELEY LABORATORY

AUG 14 1978

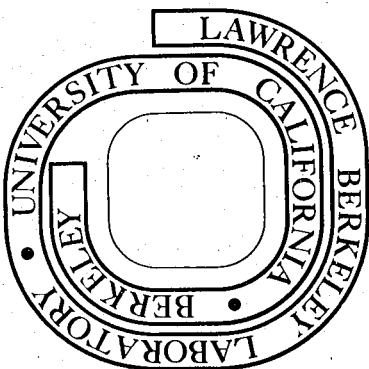
June 1978

LIBRARY AND  
DOCUMENTS SECTION

Prepared for the U. S. Department of Energy  
under Contract W-7405-ENG-48

TWO-WEEK LOAN COPY

This is a Library Circulating Copy  
which may be borrowed for two weeks.  
For a personal retention copy, call  
Tech. Info. Division, Ext. 6782



LBL-7682  
C.2

This report was done with support from the Department of Energy. Any conclusions or opinions expressed in this report represent solely those of the author(s) and not necessarily those of The Regents of the University of California, the Lawrence Berkeley Laboratory or the Department of Energy.

The Thermal Expansion of the Directionally  
Solidified Al-CuAl<sub>2</sub> Eutectic

Dennis Frank Baker  
(M. S. thesis)

June 1978

Lawrence Berkeley Laboratory  
University of California  
Berkeley, California 94720



THE THERMAL EXPANSION OF THE DIRECTIONALLY  
SOLIDIFIED  $\text{Al-CuAl}_2$  EUTECTIC

Contents

ABSTRACT . . . . .	v
I. INTRODUCTION . . . . .	1
II. THEORY . . . . .	4
III. EXPERIMENTAL . . . . .	12
A. MATERIAL PREPARATION . . . . .	12
1. Solidification . . . . .	12
2. Characterization . . . . .	16
B. SPECIMEN PREPARATION . . . . .	20
1. Determination of Dilatometer Axes and Measurement of $\lambda$ . . . . .	20
2. Machining of Dilatometer Specimens. . . . .	21
C. THERMAL EXPANSION MEASUREMENTS . . . . .	22
1. Dilatometer Apparatus . . . . .	22
2. Procedure . . . . .	24
3. Standard Measurements and Corrections . . . . .	27
IV. RESULTS . . . . .	28
A. RAW CURVES . . . . .	28
B. FINISHED CURVES . . . . .	30

V.	DISCUSSION . . . . .	31
A.	COMPARISON WITH PREDICTED VALUES AND INTERPRETATION . . . . .	31
B.	DEFICIENCIES IN THE ELASTIC MODEL. . . . .	32
C.	EFFECTS OF TEMPERATURE ON MICROSTRUCTURE . . . . .	34
	1. Coarsening . . . . .	34
	2. Precipitation . . . . .	35
D.	EFFECTS OF MICROSTRUCTURE ON THERMAL EXPANSION . . . . .	36
VI.	CONCLUSIONS . . . . .	39
VII.	ACKNOWLEDGEMENTS . . . . .	40
	REFERENCES . . . . .	41
	TABLES . . . . .	45
	FIGURES . . . . .	52

THE THERMAL EXPANSION OF THE DIRECTIONALLY  
SOLIDIFIED Al-CuAl<sub>2</sub> EUTECTIC

Dennis Frank Baker

ABSTRACT

Alloys of Al-CuAl<sub>2</sub> eutectic composition were prepared with high purity materials (99.999%) and directionally solidified horizontally in a rectangular ceramic boat at 0.96, 4.0, 8.3, 17.5, and 82.0  $\mu\text{m}/\text{sec}$  through a temperature gradient of 45  $^{\circ}\text{C}/\text{cm}$ . These ingots were examined macroscopically and the best single grain regions were selected for further measurements. From micrographs taken of the top, side and cross section of the ingot, it was found that the interlamellar spacings were 7.5, 3.5, 2.6, 1.8 and 1.4  $\mu\text{m}$  respectively, and from the measured lamellar orientation relationships specimens were machined with axes aligned in the principal lamellae coordinate directions. Transmission Laue photographs taken using Ni filtered Cu K $\alpha$  radiation verified that the texture is consistent with the crystallographic relationships

$$(121)_{\theta} \parallel (111)_{\text{Al}} ; \langle 12\bar{3} \rangle_{\theta} \parallel \langle 1\bar{2}1 \rangle_{\text{Al}}.$$

Thermal expansion was measured by standard dilatometry (Cu standard) using a set point program cycling between room temperature and 500 $^{\circ}\text{C}$ . It was found that the thermal expansion of the directionally solidified Al-CuAl<sub>2</sub> eutectic decreases with increasing inter-



lamellar spacing, is greatest in the growth direction (approximately  $\langle 1\bar{2}1 \rangle_{Al}$ , in the plane of the lamellae) least in the transverse direction (approximately  $\langle 10\bar{1} \rangle_{Al}$ , in the plane of the lamellae), and intermediate in the second transverse direction (approximately  $\langle 111 \rangle_{Al}$  normal to the lamellae).

These results confirm that the  $CuAl_2$  phase is anisotropic with respect to thermal expansion, but the interlamellar spacing dependence of thermal expansion is not predicted by any known theory of composite materials.

## I. INTRODUCTION

R. W. Kraft and D. L. Albright<sup>1</sup> were the first workers to directionally solidify the Al-CuAl<sub>2</sub> eutectic. This alloy is in the class of materials known as in situ composites, i.e., the composite as grown consists of a reinforcement phase (CuAl<sub>2</sub>) embedded in a softer matrix phase (Al solid solution) in a regular microstructure. This material has the prototype lamellar microstructure for in situ composites with better mechanical properties at higher temperatures such as in the Ni-Cb-Cr-Al system.<sup>2</sup> The principal subject studied so far besides mechanical properties<sup>3-13</sup> and the characterization of the interface<sup>3,4,5,7,9,14,21</sup> has been the characterization of the microstructure as a function of the material and solidification parameters.

Since only the Al-Cu eutectic system is investigated in this work, the materials parameters remain constant. The solidification parameters are growth velocity  $v$ , which is generally taken to be the same as the rate  $R$  that the melt is withdrawn from the furnace, and the constitutional undercooling  $\Delta T$ , which is related to the thermal gradient  $G$  at the interface. These parameters have been related to each other and to the lamellar spacing  $\lambda$  by the following relations as derived by K. A. Jackson and J. D. Hunt<sup>22</sup> following the volume diffusion approach of C. Zener.<sup>23</sup>

$$\lambda^2 v = \text{constant} \quad (1)$$

$$\Delta T^2/v = \text{constant.} \quad (2)$$

Both constants depend upon material parameters. The first relation has been verified by numerous workers<sup>24-7</sup> and also in this investigation. The undercooling is more difficult to measure, but workers<sup>28-9</sup> have confirmed this second relation for the Pb-Sn eutectic. A third criterion derived by A. S. Yue<sup>30</sup> is that

$$\frac{G}{R} \geq \frac{m C_o}{D} \left[ \frac{1-k}{k} + \frac{(T-T_o) D'}{k k} \right] \quad (3)$$

where  $m$  is the slope of the liquidus line

$C_o = C - C_E$  where  $C$  is the concentration and  $C_E$  is the eutectic composition

$k$  is the segregation constant

$K$  is the thermal diffusivity of the melt

$D$  is the diffusion coefficient in the melt

$D'$  is the thermal diffusion coefficient

$T$  is the temperature of the furnace

and  $T_o$  is the temperature of the interface.

The first term had been derived earlier by W. A. Tiller et al.,<sup>31</sup> and F. R. Mollard and M. C. Flemings.<sup>32</sup> When this criterion is not met, a microstructure described as degenerate, disordered, banded and cellular results, whereas when it is satisfied, the regular lamellar microstructure with period  $\lambda$  results. This was observed by the earliest workers.<sup>1,25</sup>

The object of this work is to measure the thermal expansion of the Al-Cu directionally solidified eutectic so as to determine its lamellar dependence and anisotropy. The universal law of composites as proposed by Zvi Hashin<sup>33</sup> does not have a lamellar spacing dependence, having only the properties of the phases and their volume fractions as parameters for determining the particular property of the composite. The approach taken in this work is to grow several different ingots with different lamellar spacings and to cut three dilatometer specimens with their axes along the principle lamellae coordinates, that is, normal to the lamellae (vertical), in the lamellae close to the growth direction (longitudinal) and in the remaining orthogonal direction in the lamellae (transverse), and measure the thermal expansion.

Little work has been reported about the thermal expansion of the Al-Cu eutectic.<sup>34</sup> The thermal expansion of the Al phase is well known.<sup>35,36</sup> However, the thermal expansion of the  $\text{CuAl}_2$ , or  $\theta$  phase, is not well known.<sup>37-8</sup>

## II. THEORY

The ideal microstructures as shown in Figure 1 is briefly described as a set of alternating planar plates consisting of the two phases, such that the extent of the plates is much greater than their thickness or spacing  $\lambda$ . The volume fractions of the two phases are nearly equal. The volume fraction of the  $\theta$  phase is 0.475, and that of the Al phase is of course 0.525.<sup>12</sup>

An universal law of composites that has been proposed Z. Hashin<sup>33</sup> is

$$\left( \frac{V_A}{K_A} + \frac{V_B}{K_B} \right)^{-1} \leq K_C \leq V_A K_A + V_B K_B \quad (4)$$

where  $V$  is the volume fraction,  $K$  is a physical property, and the subscripts A and B refer to their respective phases and C refers to the composite. This expression is independent of all microstructural parameters except volume fraction. Analogous formulas for electrical conductivity, dielectric constants, magnetic permittivity, and heat conduction are known to be valid. B. Paul<sup>39</sup> and R. Hill<sup>40</sup> have shown that the right hand side holds for elasticity. In the somewhat more elaborate derivation below, this rule of mixtures has been invoked.

In the elastic model, we have the constraint that there is no slip at the interface between the phases,<sup>3,5,12</sup> therefore the strains of the two phases in the interface are equal. Since all the surface forces are assumed to be zero, a condition of plane stress in the

lamellae exists due to the difference in the thermal expansion of the phases.

Assuming the rule of mixtures holds,<sup>33,39,40</sup> we have

$$E_C = E_{Al} V_{Al} + E_{\theta} V_{\theta} \text{ where } E \text{ is Young's modulus.} \quad (5)$$

The Duhamel-Neumann relations<sup>41</sup> are

$$\epsilon_{ij} = \frac{(1+\nu)}{E} \sigma_{ij} - \frac{\nu}{E} \delta_{ij} \sigma_{kk} + \alpha_{ij} \Delta T \quad (6a)$$

$$\sigma_{ij} = \frac{E\nu}{(1-2\nu)(1+\nu)} \epsilon_{kk} + \frac{E}{1+\nu} \epsilon_{ij} - \frac{E}{1-2\nu} \alpha_{ij} \Delta T \quad (6b)$$

where  $\sigma_{ij}$  and  $\epsilon_{ij}$  are stress and strain respectively,  $\delta_{ij}$  is Kronecker delta, and  $\alpha_{ij}$  and  $\Delta T$  are the coefficient of thermal expansion and the change in temperature. From the rule of mixtures (Eq. (4)) and the equilibrium condition that forces at a surface must total zero, one has that

$$\sigma_{ij\theta} = - \sigma_{ijAl} \frac{V_{Al}}{V_{\theta}} \quad i, j = 1, 2 \quad (7)$$

$$\sigma_{33} = 0 \quad \text{because of geometry} \quad (8)$$

$$(\sigma_{31} = \sigma_{13} = \sigma_{32} = \sigma_{23} = 0 \quad \text{also}).$$

From the condition of no slip at the interface

$$\epsilon_{ijc} = \epsilon_{ijAl} = \epsilon_{ij\theta} \quad (9)$$

$$\begin{aligned} \therefore \left( \frac{1+\nu}{E} \right)_{\theta} \sigma_{ij\theta} - \left( \frac{\nu}{E} \right)_{\theta} \delta_{ij} \sigma_{\gamma\gamma\theta} + \alpha_{ij\theta} \Delta T &= \left( \frac{1+\nu}{E} \right)_{Al} \sigma_{ijAl} \\ &- \left( \frac{\nu}{E} \right)_{Al} \delta_{ij} \sigma_{\gamma\gamma Al} + \alpha_{ijAl} \Delta T. \end{aligned} \quad (10)$$

Again invoking the rule of mixtures,

$$\sigma_{ij_c} = V_{A1} \sigma_{ij_{A1}} + V_{\theta} \sigma_{ij_{\theta}} = 0 \quad (11)$$

then from Eq. (10)

$$\begin{aligned} (\alpha_{ij_{\theta}} - \alpha_{ij_{A1}}) \Delta T = \sigma_{ij_{A1}} \left[ \left( \frac{1+\nu}{E} \right)_{A1} + \left( \frac{1+\nu}{E} \right)_{\theta} \frac{V_{A1}}{V_{\theta}} \right] \\ - \left[ \left( \frac{\nu}{E} \right)_{A1} + \left( \frac{\nu}{E} \right)_{\theta} \frac{V_{A1}}{V_{\theta}} \right] \sigma_{YY_{A1}} \delta_{ij} \end{aligned} \quad (12)$$

$$(\alpha_{\theta} - \alpha_{A1})_{ij} \Delta T = \sigma_{ij_{A1}} A - B \sigma_{YY_{A1}} \quad (13)$$

where  $i = j$  since thermal expansion is pure dilation and

$$A = \left( \frac{1+\nu}{E} \right)_{A1} + \left( \frac{1+\nu}{E} \right)_{\theta} \frac{V_{A1}}{V_{\theta}} \quad \text{and} \quad B = \left[ \left( \frac{\nu}{E} \right)_{A1} + \left( \frac{\nu}{E} \right)_{\theta} \frac{V_{A1}}{V_{\theta}} \right].$$

If one assumes that  $\sigma_{11} = \sigma_{22}$ , then

$$(\alpha_{\theta} - \alpha_{A1})_{ij} \Delta T = \left[ \left( \frac{1-\nu}{E} \right)_{A1} + \left( \frac{1-\nu}{E} \right)_{\theta} \frac{V_{A1}}{V_{\theta}} \right] \sigma_{ij_{A1}}. \quad (14)$$

Letting  $M_{A1} = (E/1-\nu)_{A1}$ ;  $M_{\theta} = (E/1-\nu)_{\theta}$ , one has Lazlo's<sup>42</sup> solution for the stress between two flat plates joined together:

$$\sigma_{ij_{A1}} = (\alpha_{\theta} - \alpha_{A1})_{ij} \Delta T \left[ \frac{M_{A1} M_{\theta} V_{\theta}}{V_{\theta} M_{\theta} + V_{A1} M_{A1}} \right] \quad (15a)$$

$$\sigma_{ij_{\theta}} = (\alpha_{A1} - \alpha_{\theta})_{ij} \Delta T \left[ \frac{M_{A1} M_{\theta} V_{A1}}{V_{\theta} M_{\theta} + V_{A1} M_{A1}} \right]. \quad (15b)$$

If  $\sigma_{11} \neq \sigma_{22}$  which is likely if  $\alpha_{11_{\theta}} \neq \alpha_{22_{\theta}}$ , then

$$\sigma_{ij_{A1}} = \frac{E_{\theta} E_{A1} V_{\theta} \Delta T}{E_{A1} V_{A1} + E_{\theta} V_{\theta}} \left[ \frac{(\alpha_{ij_{\theta}} - \alpha_{A1})(1-\nu) + \nu(\alpha_{\theta} - \alpha_{A1})}{1 - \nu^2} \frac{\delta_{ij}}{\gamma\gamma} \right] \quad (16a)$$

$$\sigma_{ij_{\theta}} = \frac{E_{\theta} E_{A1} V_{A1} \Delta T}{E_{A1} V_{A1} + E_{\theta} V_{\theta}} \left[ \frac{(\alpha_{A1} - \alpha_{ij_{\theta}})(1-\nu) + \nu(\alpha_{A1} - \alpha_{\theta})}{1 - \nu^2} \frac{\delta_{ij}}{\gamma\gamma} \right] \quad (16b)$$

$$i=j=1,2; \gamma=1,2.$$

From the condition that at the interface there is no slip, one has

$$\epsilon_{ij_c} = \alpha_{ij_c} \Delta T + \epsilon_{ij_{A1}} = \epsilon_{ij_{\theta}} \quad i = j = 1,2 \quad (17)$$

$$\epsilon_{ij_{A1}} = \frac{(\alpha_{\theta} - \alpha_{A1})}{V_{\theta} M_{\theta}} \frac{\Delta T M_{\theta} V_{\theta}}{ij} + \alpha_{ij_{A1}} \Delta T \quad (18a)$$

$$\epsilon_{ij_{\theta}} = \frac{(\alpha_{A1} - \alpha_{\theta})}{V_{\theta} M_{\theta} + V_{A1} M_{A1}} \frac{\Delta T M_{A1} V_{A1}}{ij} + \alpha_{ij_{\theta}} \Delta T. \quad (18b)$$

Thus in the plane of the lamellae, the thermal coefficients of expansion are

$$\alpha_{ij_c} = \frac{(\alpha_{\theta} - \alpha_{A1})}{V_{\theta} M_{\theta} + V_{A1} M_{A1}} \frac{M_{\theta} V_{\theta}}{ij} + \alpha_{ij_{A1}} \quad (19a)$$

$$\alpha_{ij_c} = \frac{(\alpha_{A1} - \alpha_{\theta})}{V_{\theta} M_{\theta} + V_{A1} M_{A1}} \frac{M_{A1} V_{A1}}{ij} + \alpha_{ij_{\theta}}. \quad (19b)$$

In the vertical direction, one has

$$\epsilon_{33_c} = \epsilon_{33_{A1}} \frac{V_{A1}}{V_{\theta} + V_{A1}} + \epsilon_{33_{\theta}} \frac{V_{\theta}}{V_{\theta} + V_{A1}} = \alpha_{33_c} \Delta T \quad (20)$$

$\epsilon_{33_c}$  can be found by substituting Eq. (6a) for the strains of the two phases, expressing the stresses as in Eq. (16a-b).



Finally,

$$\alpha_{33_c} = \alpha_{33_{Al}} V_{Al} + \alpha_{33_\theta} V_\theta + \frac{\nu V_\theta V_{Al} [E_{Al} - E_\theta] [2\alpha_{Al} - \alpha_{11_\theta} \alpha_{22_\theta}]}{(E_{Al} V_{Al} + E_\theta V_\theta) (1-\nu)} \quad (21)$$

since the thermal expansion of aluminum isotropic.

In summary then, the matrix stresses due to the difference in thermal expansion can be written

$$\sigma_{long_{Al}} = \sigma_{11_{Al}} = \frac{E_\theta E_{Al} V_\theta \Delta T}{E_{Al} V_{Al} + E_\theta V_\theta} \left\{ \frac{(\alpha_{long_\theta} - \alpha_{Al}) + \nu (\alpha_{trans_\theta} - \alpha_{Al})}{1 - \nu^2} \right\} \quad (22a)$$

$$\sigma_{trans_{Al}} = \sigma_{22_{Al}} = \frac{E_\theta E_{Al} V_\theta \Delta T}{E_{Al} V_{Al} + E_\theta V_\theta} \left\{ \frac{(\alpha_{trans_\theta} - \alpha_{Al}) + \nu (\alpha_{long_\theta} - \alpha_{Al})}{1 - \nu^2} \right\} \quad (22b)$$

$$\sigma_{vertical_{Al}} = \sigma_{33_{Al}} = 0. \quad (22c)$$

The thermal expansion of the composite can be written thus in terms of Figure 1:

$$\epsilon_{11_c} = \alpha_{long_c} \Delta T = \left[ \frac{(\alpha_{long_\theta} - \alpha_{Al}) M_\theta V_\theta + \alpha_{Al}}{V_\theta M_\theta + V_{Al} M_{Al}} \right] \Delta T \quad (23a)$$

$$\epsilon_{22_c} = \alpha_{trans_c} \Delta T = \left[ \frac{(\alpha_{trans_\theta} - \alpha_{Al}) M_\theta V_\theta + \alpha_{Al}}{V_\theta M_\theta + V_{Al} M_{Al}} \right] \Delta T \quad (23b)$$

$$\epsilon_{33_c} = \alpha_{vertical_c} \Delta T = \left\{ \alpha_{Al} V_{Al} + \alpha_{vertical_\theta} V_\theta + \frac{\nu V_\theta V_{Al} [E_{Al} - E_\theta] [2\alpha_{Al} - \alpha_{long_\theta} - \alpha_{trans_\theta}]}{(1-\nu) (E_{Al} V_{Al} + E_\theta V_\theta)} \right\} \Delta T. \quad (23c)$$

The above equations have been derived assuming that both the Al and  $\theta$  phases are elastically isotropic and that Poisson's ratio  $\nu$  for the  $\theta$  phase and the Al phase are the same. Notice that the equations for thermal expansion fall nearly into the universal law of composites formulation, except for terms that can be categorized as accounting for Poisson effects.

It is extremely difficult to grow single crystals of  $\text{CuAl}_2$ . Most of the single crystal work done on this material has been done on material imbedded in the directionally solidified eutectic. Tensile strength of the directionally solidified eutectic is a function only of the angle the tensile axis makes with the lamellar plane. A. S. Yue et al.<sup>3</sup> show that Young's modulus of the eutectic does not vary significantly ( $\pm 10\%$ ) with orientation, as does S. Justi.<sup>67</sup> R. W. Hertzberg, F. D. Lemkey, and J. A. Ford through microbend tests obtained the same results. Considering that Young's modulus varies over  $\pm 10\%$  with direction for the Al phase,<sup>43</sup> one can conclude that the anisotropy of the  $\theta$  phase is nearly the same as for Al. The assumption that both Al and  $\theta$  are elastically isotropic can be considered a good approximation.

The mechanical properties of the  $\theta$  phase are not well known at high temperatures. It is known that the hardness at  $500^\circ\text{C}$  is 10% of the hardness at room temperature and that  $\theta$  can be extruded successfully at  $440^\circ\text{C}$ .<sup>44</sup> The mode of fracture in the  $\theta$  phase is known to be brittle at room temperature but ductile at higher temperatures ( $\sim 300^\circ\text{C}$ ).<sup>8</sup>

Young's modulus for aluminum has been measured dynamically at high temperatures by R. F. Wilde and N. J. Grant.<sup>45</sup> They found  $E_{\text{Al}}$  to

be  $67.6 \text{ GN/m}^2$  ( $9.8 \times 10^6 \text{ psi}$ ) at room temperature and  $53.8 \text{ GN/m}^2$  ( $7.8 \times 10^6 \text{ psi}$ ) at  $427^\circ\text{C}$  ( $800^\circ\text{F}$ ). Noting that the thermal expansion as derived in Eq. 23a-c is a function of the ratio of Young's modulus for the  $\theta$  and  $\text{Al}$  phases, it is assumed that this ratio is independent of temperature, since  $E_\theta(T)$  cannot increase as  $T$  increases, and it is unlikely that  $E_\theta \leq E_{\text{Al}}$ .

For the purpose of making calculations, it will be assumed that any temperature dependence of  $\bar{\alpha}_\theta$  is independent of orientation, so that it may be approximated by the polycrystalline data of D. M. Rabkin, V. R. Ryabov, A. V. Lozovskaya, and V. A. Dorzhenko<sup>37</sup> by taking the mean coefficient of thermal expansion at lower temperatures to be a fraction of that measured at  $500^\circ\text{C}$ , for which<sup>38</sup>

$$\begin{aligned}\bar{\alpha}_{100} &= \bar{\alpha}_{010} = 16.5 \times 10^{-6} \text{ }^\circ\text{C}^{-1} \\ \bar{\alpha}_{001} &= 24.5 \times 10^{-6} \text{ }^\circ\text{C}^{-1}.\end{aligned}$$

Since the growth direction is approximately  $[12\bar{3}]_\theta$  and the vertical direction (lamellae normal) is  $[121]_\theta$ <sup>3,4,5,7,9,14-21</sup> the thermal expansion of the  $\theta$  phase in the eutectic along the principle axes of the lamellae can be calculated. The literature thermal coefficients to be used in the calculations are listed in Table 1. A. Pattnaik's and A. Lawley's<sup>12</sup> values for  $E_\theta$  ( $99.3 \text{ GN/m}^2$  or  $14.4 \times 10^6 \text{ psi}$ ) and  $E_{\text{Al}}$  ( $75.2 \text{ GN/m}^2$  or  $10.9 \times 10^6 \text{ psi}$ ) will be used. It is assumed that  $v_{\text{Al}} = v_\theta = 0.33$  as B. Cantor and G. A. Chadwick<sup>7</sup> have done. The volume fractions have been assumed constant, though this is only approximately true, as will be discussed later.

Table 2 is a table of the calculated thermal expansion values for the composite to be used for comparison with the experimental results. They are plotted in Figure 34. The prediction according to theory is that the longitudinal direction thermal expansion should be greatest, that the thermal expansion in the transverse direction should be least, and that thermal expansion in the vertical direction should be slightly greater than thermal expansion in the transverse direction.

Using the universal law of composites directly results in a narrower range of values that  $\bar{\alpha}_c$  can take.

The shortcomings of the model, aside from microstructural defects, are that other temperature effects and mechanical phenomena are not fully appreciated.

### III. EXPERIMENTAL

#### A. MATERIAL PREPARATION

##### 1. Solidification

Briefly, a charge of alloy is melted in an alumina boat and slowly drawn out of a horizontal tube furnace and thus directionally solidified as shown in Figure 2.

A charge is material that has been cut from a master ingot (and its surface relatively smoothed out by milling). The shape of the charge should approximate that of the boat because the melted charge does not flow readily, apparently due to high surface tension. The master ingot consists of 33.25 w/o Cu-Al made from 99.999% Cu and 99.999% Al by inductively melting and stirring them together in a zirconia crucible and casting them into a massive Cu mold.

The boats used in this work are made of Norton Alundum, AL788, and are known as combustion boats. The particular model used has outside measurements of 25.4 cm (10") long, 2.5 cm (1") wide at the open top, 1.3 cm (1/2") wide at the bottom, and 1.4 cm (9/16") high with a wall width of 3 mm (1/8"). The end of the boat is cut off square with a diamond saw. A slot 1.5 mm (1/16")  $\times$  1.5 mm (1/16")  $\times$  10 cm (4") is similarly cut down the center of the boat for the thermocouple used to determine the melt temperature.

A type K (chromel-alumel) 0.25 mm (10 mil) thermocouple in a 2-hole 0.38 mm (15 mil) mullite insulator tube (Coors) is placed in the slot and covered with Ceramobond, a high temperature, low porosity,

ceramic adhesive and coating. A smooth continuous surface is maintained in the bottom of the boat.

The boat is fitted into a carbon block water cooled chiller.<sup>46</sup> The whole assembly is then mounted in a fused quartz tube 91.4 cm (36") long, 45 mm (1.75") OD with a 3 mm (0.10") wall width. A nut and screw at the handle end of the boat is used to level it. The quartz tube is mounted between two brackets, one end leading to the mechanical pump, and the other end open, so as to be fitted with a cap on the chiller assembly which contains the water feedthroughs to the chiller and the thermocouple feedthrough as shown in Figure 3. To prevent fracture of the quartz tube due to thermal expansion, both ends are water cooled at the brackets.

The furnace is 30.5 cm (12") OD, 7.6 cm (3") ID, and 45.7 cm (18") long. It is wound with 40% RH-Pt furnace wire. A Typo K thermocouple is used to monitor the core temperature, with a second Type K thermocouple also in the core as a safety precaution against overheating. One end of the furnace is water cooled by a copper insert extending inside the furnace.<sup>46</sup>

After placing the charge in the boat and placing the chiller assembly and boat in the quartz tube and sealing the tube by tightening the screws in the cap to snug the cap against an O-ring, the tube is evacuated by a mechanical pump to a pressure of less than 50  $\mu$ m Hg. The quartz tube is then flushed with Ar to a slightly positive pressure, and then pumped out again. This is repeated at least three times. Directional solidification is done under a slightly positive pressure of Ar.

Heating of the furnace can start while it is pumped out and flushed out with Ar. This procedure provides a final check for the thermocouple connections leading to the boat (it is easy to cross connect the thermocouple wires because the identifying red and yellow insulation will soon burn off, and the difference in the stiffness of the wires is not always perceived well enough to tell the difference). Also, the higher temperature of the directional solidification apparatus allows all the surfaces to outgas a bit better so that a better inert gas atmosphere is finally obtained. Some time can also be saved because it takes time for the furnace to heat up to the final ambient temperature. One should not exceed the current ratings for the furnace because the capacity of the power supply may be exceeded but more importantly the furnace wire may heat up so fast that not enough heat can be conducted away to keep the furnace wire itself from melting and creating an open circuit. This catastrophe necessitates rewinding the furnace with new wire, though the furnace can be shorted across the "dead" part, but this measure is not recommended.

The furnace is heated to the temperature of  $1000^{\circ}\text{C}$  as read by the furnace monitoring thermocouple where it can be set for the remainder of the run by means of a controlling thermocouple feedback circuit to the power supply. The thermocouple measuring the temperature of the melt should read the same or a few degrees less. The furnace is held at this ambient temperature  $T_0$  until the furnace comes to equilibrium, i.e., the temperature of the boat no longer changes. This usually takes an hour or so after the furnace controlling thermocouple measures  $T_0$ .

Once the furnace has come to equilibrium, the furnace is ready to be slowly and steadily drawn away from around the boat. The rate at which this is done is determined by a pair of gear boxes in series connected by simple pulleys to the furnace as shown in Figure 3. The gears are powered by an electric motor, the speed of which is controlled by a resistor box. A regulated power supply supplies the power to the electric motor through the regulated the resistor box. Not surprisingly the speed the furnace moves for a given gear setting varies linearly with the resistor box settings. Thus a continuous range of furnace rates is available. The upper bound is limited by the maximum rate that heat can be withdrawn from the melted charge. The lower bound is limited by practical consideration of the length of time to solidify the ingot. These maximum and minimum furnace rates are about  $90 \mu\text{ms}^{-1}$  and  $0.6 \mu\text{ms}^{-1}$  respectively.

The rates used for the five ingots solidified in this investigation were 0.96, 4.0, 17.5, and  $82.0 \cdot 10^{-4} \text{cm/sec}$ . These ingots were later found to have lamellar spacings of 7.5, 3.5, 2.6, 1.8, and  $1.4 \mu\text{m}$  respectively. Figure 4 confirms that  $\lambda^2 v = \text{const.}$  as predicted by theory.

The thermal gradient  $G$  can be determined by measuring the slope of a curve marked by a pen on a chart recorder with the emf of the Type K thermocouple as a function of time. Temperature and the emf generated by a Type K thermocouple have a nearly linear relationship. Given the rate the paper moves, the rate the furnace is withdrawn (calculated by noting time and the position of a pointer fixed to the



furnace on a fixed scale beside the furnace track), the thermal gradient can be calculated. Also, the gradient can be calculated by noting the temperatures and making the calculations directly (assuming linearity) when the rate of the furnace is determined. The thermal gradient  $G$  for most of the ingots directionally solidified in this work was about  $45^{\circ}\text{C}/\text{cm}$ .

## 2. Characterization

After the ingot is removed from the boat, it is squared up on a milling machine, i.e., the top of the ingot is leveled, and flat parallel surfaces are milled on the sides of the ingot. The bottom of an ingot is the best reference surface, but this is not ideal because the Ceramobond covering the thermocouple slot in the boat may not have been ideally smooth. Even though the bottom of the boat is planar, the bottom surface of the ingot is convex. The top surface of the ingot is not flat because the charge will not flow and evenly distribute in the boat due to high surface tension.

The whole ingot is then polished along the top and a side surface through four grades of emery paper (0,00,000,0000), rotating the ingot  $90^{\circ}$  and washing between papers, using kerosene as a lubricant. Then these large surfaces are polished by hand on a  $1\text{ }\mu\text{m}$  diamond wheel to remove a majority of scratches. The whole ingot is then immersed into a dilute solution of Keller's etch. The whole grain structure of the ingot is thereby revealed and the extent of the single grain regions can be surmised, and thus it can be determined whether an acceptably large single grain has been produced. Typically only about 50-60% of the ingot is a

good single crystal region suitable for use in this experiment. The end of the ingot which freezes first is polycrystalline. Farther along the ingot, a single grain finally grows large enough to exclude the other grains, and at the tail end of the ingot, the microstructure is again polycrystalline.

Figures 5-9 are rough sketches of the macrostructures of the ingots from which specimens were taken for this work. Note that the length of "good" crystal as well as its width and height decrease as the lamellar spacing decreases, until for the smallest spacing, the macrostructure appears uniform because of the large quantity of grains. Figure 9 shows the generalized characteristics of the grains, greatly exaggerated. This macrostructure does tend to have the lamellae oriented in the growth direction. The direction of the hatched lines in Figures 5-8 indicates the general projection of the lamellae for the particular view. Solid lines drawn across the sketches show the parts from which particular dilatometer specimens were cut.

After examining the ingots to determine the macrostructure, the parts of the ingot from which the dilatometer specimens will be cut are then spark cut (to save material) from the ingot. The pieces are then mounted in Koldmount, a self-curing resin, and polished through the four grades of emery papers (0, 000, 0000) making sure to turn the specimens  $90^{\circ}$  from paper to paper, and washing thoroughly between papers so as not to bring the larger grit down to the new paper from the previous one. The specimens are then polished on a  $1\text{ }\mu\text{m}$  diamond wheel. When no scratches are visible to the unaided eye, about 20 minutes of polishing in a Leco  $0.05\text{ }\mu\text{m}$  grit (cerium oxide) slurry will finish the

polishing. The specimens are then etched for about 3 seconds in the strong Keller's etch solution by immersion. A dilute solution will not etch evenly, and spots and splotches will be evident.

The ideal microstructure for the directionally solidified eutectic is flat planar sheets of alternating phases bound fast to one another. An example of a near ideal microstructure is Figure 10.

One of the defects that occurs commonly in the microstructure is called a "dislocation" by analogy with a defect for planes of atoms in metals. In this defect, one of the lamellae ends abruptly (as seen in the surface of a specimen). Figure 11 shows numerous dislocations. A fault line is defined by the great number of dislocations along it. Dislocations are formed due to small perturbations in the solidification parameters of composition, growth rate, and undercooling.<sup>22,47</sup> Generally the density of defects increases with decreasing lamellar spacing.

The lamellae also tend to shift in orientation with respect to ingot coordinates. Figure 12 shows that the extremum orientations can be as much as  $20^{\circ}$  apart. These variations are due in part to the fact that the heat gradient in the furnace during freezing of the ingot is not constant, but varies slightly with position in the melt.

Figure 13 shows that all the defects are magnified by a factor of  $1/\sin \theta$ , where  $\theta$  is the angle between the normal of the lamellae and the normal of the polished surface.

The ingot with a lamellar spacing of  $1.4 \mu\text{m}$  was polycrystalline, consisting of elongated needle-like crystals along the growth direction (Figures 14a-b). The degenerate structure is an indication that the composition of the specimen is slightly off eutectic, or that some small

amount of impurity is present.

Laue transmission photographs were taken to verify that the texture of the Al-CuAl<sub>2</sub> directionally solidified eutectic is consistent with the crystallographic relation  $(111)_{\text{Al}} \parallel (121)_{\theta}$ ,  $\langle 10\bar{1} \rangle_{\text{Al}} \parallel \langle 1\bar{1}0 \rangle_{\theta}$  with the growth direction approximately  $\langle 1\bar{2}1 \rangle_{\text{Al}} \parallel \langle 12\bar{3} \rangle_{\theta}$  as first found by R. W. Kraft and A. L. Albright<sup>18,19</sup> and shown by L. Valero<sup>49</sup> and others.<sup>3,5,7,9</sup>

A transverse slab where the normal coincides with the growth direction, is cut off with a diamond wheel about 0.50 mm thick, and mechanically thinned down to about 0.12 mm, which is approximately  $2 \mu t$  for Cu K<sub>α</sub> radiation ( $\mu$  is the linear absorption coefficient and  $t$  is the thickness). Specimens thinner than this are not self supporting. If the face of the specimen to be cut is polished and etched before being cut, then the macrostructure of the ingot can be seen, and thus the orientation of each grain individually can be determined. Etching one side of the slice is also a method of marking which side is which.

The transmission Laue photographs were made by mounting the specimen on a goniometer with the top of the ingot up and the growth direction toward the beam. The specimen-film distance was 3 cm. Cu K<sub>α</sub> filtered radiation was used. A typical transmission Laue photograph is shown in Figure 15.

Figures 16-19 are stereographic projection plots of Laue photographs. Figures 16-18 are superpositions of two photographs taken a few millimeters apart in the same specimen. If two or more reflections can be identified for a phase, its orientation can be determined. Figures 16-19 verify that the crystallographic orientation of the ingot was that

found by Kraft<sup>18,19</sup> and Valero<sup>49</sup>.

The Laue photographs for the ingot having a lamellar spacing of 1.4  $\mu\text{m}$  showed that the ingot is polycrystalline as was evident in Figures 14a and b. The Laue photographs for this ingot did not show continuous rings, but that there were several grains in the x-ray rings, but that there were several grains in the x-ray beam. It was impossible to determine which reflections belonged to which of the several grains, but all of the observed arcs are consistent with the ideal growth direction of  $\langle 1\bar{2}1 \rangle_{\text{Al}} \parallel \langle 12\bar{3} \rangle_{\theta}$ .

## B. SPECIMEN PREPARATION

### 1. Determination of Dilatometer Axes and Measurement of $\lambda$

The lamellar orientation can be calculated by finding the normal to the lamellae. From the three polished surfaces, one can take the vector cross product of the vectors lying along the average projection of the lamellae on the polished surfaces. Thus one has a set of three calculated lamellae normals which should closely agree. Table 3 gives the average lamellar normals of the ingots plotted on the stereographic projections (Figure 17-20) and used in machining the dilatometer specimens. All of the normals lie far away from the growth direction is expected.

To determine the lamellar spacing  $\lambda$  in the general case, one can use the inclinations and the spacing of the lamellae as projected on the micrographs to generate the five parameters in the following formula<sup>48</sup> as shown in Figure 20:

$$\lambda = (d_1 + d_2) \sin \left\{ \cos^{-1} \left[ \frac{\overline{SD}^2 + \overline{DC}^2 - \overline{SC}^2}{2\overline{SD} \times \overline{DC}} \right] \right\} \quad (24)$$

$$\overline{SD} = SB \sin \theta_1$$

$$\overline{DC} = \overline{BD} \tan \theta_4 = \overline{SB} \cos \theta_1 \tan \theta_4$$

$$\overline{SC} = (\overline{SB}^2 + \overline{BC}^2 - 2\overline{SB} \times \overline{BC} \cos \theta_2)^{1/2}$$

where  $\theta_1$  is the angle between the edge and projection of the lamellae on the first surface,  $\theta_2$  is the angle between the edge and projection of the lamellae on the second surface,  $\theta_4$  is the angle between the projections of the lamellae, and  $d_1$  and  $d_2$  are directly measurable on the first surface. If the surfaces are at right angles to each other, then finding  $\lambda$  is much simplified. One may find the lamellae normal as before and then calculate what lamellae spacing will give the projected lamellae spacing. Results are best when the normal lies nearly in the surface, because the difference between the projected spacing and  $\lambda$  itself will be minimal.

## 2. Machining of Dilatometer Specimens

Once the orientation of the lamellae in an ingot have been determined, a piece of the ingot can be machined into a dilatometer specimen.

The dilatometer axes are chosen to coincide with the average normal of the lamellae (vertical), a direction in the plane of the lamellae closest to the growth direction (longitudinal) and the remaining direction in the plane of the lamellae (transverse). Since the specimen with a lamellar spacing of 1.4  $\mu\text{m}$  is polycrystalline, the

dilatometer axes in this case were the ingot principal axes, with the growth direction the longitudinal direction, and the vertical and transverse ingot principal axes the dilatometer specimens' vertical and transverse axes respectively.

Dilatometer specimens are made by machining a parallelepiped of square cross section as in Figure 21 with angles  $\psi_b$  and  $\psi_c$  as determined by the dilatometer axis with the other two minor axes from a piece of the ingot with the parallel and orthogonal surfaces of a rectangular prism. These "square" parallelepipeds can be held in a square collet and turned down and faced off on both ends to give the finished dilatometer specimen ready for drilling a blind hole for the thermocouple.

## C. THERMAL EXPANSION MEASUREMENTS

### 1. Dilatometer Apparatus

The instrument used to measure thermal expansion in this experiment is known as a Theta IIIR dilatometer. Its principle parts are: a measuring head, low thermal expansion rods on either side of the specimen, a heater, and a temperature measuring device (thermocouple). The specimen chamber is shown in Figure 22.

The measuring head consists of a hermetically sealed linear voltage differential transformer (LVDT) transducer with a sensitivity of  $1 \times 10^{-5}$  cm (experimentally) and a range of 0.125 cm and an accuracy of  $5 \times 10^{-5}$  cm for this range. A massive Invar rod is connected to the measuring head. The movement of the rod to the measuring head is controlled by a set of cantilever springs. At the other end of the Invar rod a knurled nut containing set screws can be screwed on. The set screws can

be tightened to hold a fused quartz rod rigidly. A second fused quartz rod is held in a metal clamp held fixed by a lucite rod.

This whole assembly so far described slides on a track so that the specimen may be placed between the fused quartz rods and then slide inside the induction radiation (IR) coils used to heat the specimen inductively. These coils are kept cool by water flowing through them.

The specimen itself is a right cylinder. The diameter ranged from 4.75 mm to 6.35 mm. The length ranged from 6.35 mm to 14.30 mm. The controlling factors for these dimensions were the finite size of the ingots from which the specimens were taken the dimensions of the IR coils.

Temperature is measured by a Type S 10% Rh-Pt thermocouple which generates an emf which can be translated to a temperature reading within  $0.5^{\circ}\text{C}$  of the true temperature. Due to the temperature recording system (chart recorder), temperature can only be read to within  $2^{\circ}$  of the true temperature. The legs of this thermocouple are spot welded together. A blind hole large enough to accept the thermocouple bead is drilled into each specimen, the thermocouple bead inserted, and the edge of the hole peened lightly so that the thermocouple will be held in place.

Measurements are made under a reduced pressure of about  $10\text{ }\mu\text{m}$  Hg achieved with a mechanical pump. This is done to ensure that the specimen integrity is maintained by avoiding excessive buildup of oxide films and other contaminants.



## 2. Procedure

There are two methods or procedures for thermal expansion measurements: the continuous method and the set point method.<sup>50</sup> The continuous method is usually faster (even if the maximum heating and cooling rate is only 2°C/min to cut back on thermal lag between the measured temperature and the temperature the specimen actually experiences) and can be used to directly determine  $\Delta L/L$  as a function of temperature merely by plotting the dilatation and temperature directly as the ordinate and abscissa on a chart recorder.

The set point method is more accurate as the density of set points is increased. Consequently for good measurements, it will take longer than the continuous method. The set point method eliminates concern about thermal lag, since no measurements are read until the temperature equilibrates. Also, isothermal changes in length can be discerned to some extent, while they would be completely obscured in the continuous method.

The set point method was chosen because of this last consideration: It was observed in preliminary runs that a directionally solidified specimen when heated above  $\sim 230^\circ\text{C}$  would deform isothermally. This deformation has been attributed to the softening of both the Al and  $\text{CuAl}_2$  phases and the fact that the specimen is spring-loaded between the fused quartz rods. Hence, if there is a small misalignment of the quartz rods, or of the surfaces of the specimen or a combination of both, a small portion of the total surface bears all the force of the springs, and thus deforms locally. Even with the best alignment, some deformation

could occur because of surface roughness of the specimen and quartz rods. If the surface roughness of the four surfaces is each, say,  $15\text{ }\mu\text{m}$ , then the observed shrinkage for a maximum mismatch could be as great as  $30\text{ }\mu\text{m}$  or 1.2 mils.

The set point method was put into effect by scribing a program on a Datatrak drum. The Datatrak system consists of a wooden drum around which a plastic sheet is wrapped. One side of the plastic sheet is covered with a conductive film. The program is determined by a continuous scribed line. A servo driven by a magnetic sensor follows the scribed line marking the change in electrical potential.

The specimen and heater furnace controlling thermocouple emf must match an emf which is a function of position of the servo driven sensor. The heater power supply will supply power as a roughly linear function of the difference between the Datatrak emf and the specimen thermocouple emf if the difference is positive, or shut off if the difference is negative. The speed at which the program is executed depends on how fast an electric motor turns the drum. The program scribed on the plastic sheet is for set points at  $\sim 20^{\circ}\text{C}$  intervals with holds as determined from preliminary runs long enough to ensure that the specimen will come to equilibrium.

These hold times for increasing temperatures are

less than $230^{\circ}\text{C}$	$\sim 3\text{ }1/2\text{ min.}$
more than $230^{\circ}\text{C}$	$\sim 6\text{ min,}$

and for decreasing temperatures are

greater than 100°C	~ 3 min.
less than 100°C	~ 3 min.

Because the specimen takes so long to cool in a vacuum at temperatures less than 100°C, running times, that is, the time it takes to move through a set point to the next one, are of the order of 15 min. Variations in holding times are due to the small errors in scribing the program, and the "stepping" of the electric motor that turns the drum at these slow speeds (1 rev/6 hours). A run consists of two revolutions of the drum. The reason for longer times at temperature greater than 230°C for increasing temperatures is that it is at approximately this temperature that deformation of the specimen due to misalignment, mismatch, etc. first becomes apparent. Holding times were long enough so that most of the deformation due to softening of the material had occurred before the temperature was increased to the next set point.

Figure 23 is a section of a raw data chart recording.

It should be noted that the response of the heater was not to generate the temperatures the program was scribed for, but for ~10°C lower. Also, not enough time for cooling in vacuum was allowed for some of the lower temperatures less than 100°C. The cooling time is a function of temperature, and is approximately an exponential function of the difference between the specimen temperature and room temperature since heat is conducted out of the specimen primarily but not exclusively through the fused quartz rods.

### 3. Standard Measurements and Corrections

The dilatometer has to be calibrated with a known standard material, in this case 99.999% Cu. (Because of the deformation problems aforementioned, data obtained with 99.999% Al did not reproduce well.) The difference between the experimental data and accepted value is the correction function as shown in Figure 24. The correction function contains all the deviations from the accepted value for thermal expansion of Cu.<sup>65</sup> The principal component term is due to the thermal expansion of the quartz rods themselves. Experimentally the correction function was approximated as a linear function of temperature with a slope of  $2.5 \times 10^{-6} \text{ cm/}^\circ\text{C}$ . This slope is of the correct order of magnitude for the length of quartz rod involved, that is

$$\begin{aligned} \text{slope} &= \frac{1}{2} (\alpha L_{\text{eff}}) + \dots &= \frac{1}{2} (0.55 \times 15^{6.9} \text{ cm}) \\ &\text{fused quartz} &= 2.4 \times 10^{-6} \text{ cm/}^\circ\text{C}. \end{aligned}$$

The factor 1/2 is included to average change in temperature in the rods from the specimen temperature to room temperature.  $L_{\text{eff}}$  is the effective sum of the fused quartz push rods.  $\alpha$  is the mean coefficient of thermal expansion for fused quartz.<sup>66</sup>

#### IV. RESULTS

##### A. RAW CURVES

The raw curves have been qualitatively divided into four groups, depending on how tightly the curves for each cycle of both increasing and decreasing temperatures were grouped together. Ideally, all the curves should overlap each other. There were two such runs where the curves were tightly grouped together. There were five runs in which the curves were only moderately tightly grouped together, mostly due to the small amount of isothermal deformation occurring at higher temperatures especially during the first high temperature cycle. The curves at low temperatures tend to overlap each other. The largest classification (loose) of seven runs was that group where large amounts of isothermal deformation occurred in the first high temperature cycle, very little in the second high temperature cycle, and no deformation in the second low temperature cycle. Figure 25 is a typical representative of this group. There was a single case where isothermal deformation occurred at higher temperatures in all cycles, so that the curves were very loosely grouped together. These results have been tabulated in Table 4.

Qualitatively, there is a very weak trend for more isothermal deformation in the dilatometer specimens as  $\lambda$  decreases. A stronger trend is that for a given lamellar spacing, the longitudinal direction raw data is always grouped as tightly or more tightly together than the vertical direction raw data, which is as tightly or more tightly grouped

together than the data for the transverse direction, with only a single exception. The amount of deformation due to misalignment and surface roughness should be considered a random source of error. This trend is an indication of the relative compressive strengths of the eutectic in the three orthogonal directions at high temperatures.

Partially because of the problem of isothermal deformation, no definite pattern of hysteresis was found.

The finished curves are derived from the raw curves by first adding back in the isothermal deformation. Then a local coefficient of thermal expansion, calculated over a change of temperature of  $\sim 60^{\circ}\text{C}$  centered over a specific  $20^{\circ}\text{C}$  interval is used to calculate the thermal expansion that occurs in that specific  $20^{\circ}\text{C}$  interval. This is a compromise between precision and sensitivity. Then the thermal expansion for all the same specific  $20^{\circ}\text{C}$  intervals are averaged together for both increasing and decreasing temperatures. The average thermal expansions for specific  $20^{\circ}\text{C}$  intervals are added together to build a smooth curve from which the correction factor is subtracted to get the finished curve. Some extrapolation was necessary over  $\sim 20^{\circ}\text{C}$  to room temperature because of the cooling time problems in vacuum and to  $500^{\circ}\text{C}$  because of the shortfall in the Datatrak program. The standard deviation for the thermal expansion at  $500^{\circ}\text{C}$  is plotted on the finished curves as error bars. Because of the way the curve was constructed, these error bars are greater than for any other point on the curve.

## B. FINISHED CURVES

The results of this work are briefly summarized in Table 5 and in Figures 26-33.

The first general trend that should be noticed in Figures 26-30 is that the greatest thermal expansion occurs in the longitudinal direction, i.e., near the growth direction, that the least thermal expansion is in the transverse direction, and that the thermal expansion in the vertical direction is slightly greater than it is in the transverse direction as predicted. In the polycrystalline specimen with a lamellar spacing of 1.4  $\mu\text{m}$ , the vertical and transverse directions are not well defined. Since the thermal expansion of the aluminum solid solution is isotropic, the anisotropy of the thermal expansion of the composite must be due to the anisotropic thermal expansion of the  $\theta$  phase.

The second trend that should be noticed is that the thermal expansion of the composite is a function of the lamellar spacing. As can be seen from Figures 31-33, thermal expansion in all three directions is generally least for large lamellar spacings, and increases as  $\lambda$  decreases.

## V. DISCUSSION

### A. COMPARISON WITH PREDICTED VALUES AND INTERPRETATION

The most significant finding of this study is that the thermal expansion of the Al-CuAl<sub>2</sub> directionally solidified eutectic varies with interlamellar spacing. This phenomenon is not considered in any known theoretical treatment of composite materials, such as the rule of mixtures.

It should be observed that for the slowest growth rate the thermal expansion of the composite is approximately equal to that calculated in Table 1 from the reported values for the  $\theta$  phase alone, and that the intermediate values generally lie between values for the  $\theta$  phase and those predicted by the elastic rule of mixtures model as tabulated in Table 2.

An empirical approach to the interpretation of these findings other than using a more detailed and/or other continuum mechanics model, is to consider the mechanical properties of the composite as a function of  $\lambda$  and of temperature.

As a function of the lamellar spacing, yield stress,<sup>10,11,63</sup> as well as hardness<sup>9,11</sup> and elastic modulus,<sup>67</sup> increase as  $\lambda$  decreases. This indicates that the Al phase bears more of the load as  $\lambda$  decreases if the effective yield stress of the  $\theta$  phase remains the same.

The constraint in the composite is that at the interface no slip occurs.<sup>3,5,12</sup> Therefore thermal stress builds up at the lamellar interface and across both lamellae. The Al phase will yield when its yield



stress is reached. If the yield stresses of the composite increases as  $\lambda$  decreases, then the Al phase can bear larger thermal stresses (and consequently larger changes in temperature) before plastic deformation occurs. This establishes that the thermal expansion of the Al phase could conform almost immediately (small  $\Delta T$ ) to that of the  $\theta$  phase for large  $\lambda$ , but that the elastic model should be more correct as  $\lambda$  decreases.

The minimum and maximum of the thermal expansion of the composite are approximately equal to those of the  $\theta$  phase and values as predicted by the elastic rule of mixtures model, respectively. However, since thermal stress is a function of the difference in thermal expansion between the two phases rather than additive, it is unclear what function of  $\lambda$  should be used to represent the thermal expansion of the composite. No mechanical property of the composite has yet been shown to be consistently predicted by a specific function of  $\lambda$ .<sup>6</sup>

#### B. DEFICIENCIES IN THE ELASTIC MODEL

There are several phenomena that are neglected by the elastic rule of mixtures model, which will be mentioned here. They are plasticity, creep, work hardening, annealing, and thermal cycling.

Due to the difference in thermal expansion of the phases, thermal stress builds up in both lamellae as the temperature changes. If the total stress in the lamellae (thermal stress plus any residual stress) exceeds the yield strength of the phase, plastic deformation, rather than exclusively elastic strain, will occur. For the aluminum solid solution, this will occur for a temperature change of about 300°C

from room temperature in the transverse direction using the yield strength of aluminum at room temperature. Of course, the yield strength itself is a function of temperature such that near the melting point of the eutectic, plastic deformation occurs for small temperature changes.

Even if plastic deformation does not occur during the experiment, creep or relaxation will occur. The aluminum phase will tend to relax under steady state conditions until some low residual stress state is reached. Creep is greatly accelerated at higher temperatures.

In addition, the aluminum solid solution is known to work harden as it is deformed. This effect will tend to be offset at higher temperatures as the aluminum is annealing at these temperatures.

Damage to the microstructure of composites can occur because of repeated cycling of the thermal stresses in the composite by raising and lowering its temperature. Thermal cycling can be ignored in this work because of the large number of cycles ( $\sim 10^4$ )<sup>52</sup> needed for thermal cycling damage to the microstructure to be evident.

The thermal history of the specimen has generally been ignored in this work.

G. Garmon<sup>51</sup> has attempted to model this system to account for plastic deformation, creep and thermal cycling; however, he could not supply direct evidence for his standard linear solid model, which works well for the Al-NiAl<sub>3</sub> directionally solidified composite (fibrous). One could use his approach and take advantage of the fact that the microstructure allows one to assume plane stress conditions, and thus

one can use an Airy's stress function to map out elastic properties analytically.

## C. EFFECTS OF TEMPERATURE ON MICROSTRUCTURE

### 1. Coarsening

At high temperatures, the directionally solidified Al-CuAl<sub>2</sub> eutectic will coarsen, i.e., the  $\theta$  lamellae will become thicker and shorter, and begin to spheroidize.

Y. G. Nakagawa, G. C. Weatherly, and E. Ho<sup>53</sup> have advanced a theory based on the grain boundary grooving diffusion model of W. W. Mullins,<sup>54-55</sup> using a continuous coordinate system to describe a lamella at its termination. According to their theory, the rate at which the lamellae coarsen is inversely proportional to  $\lambda^2$ . This result is in qualitative agreement with the results of L. D. Graham and R. W. Kraft.<sup>56</sup> The rate of coarsening also increases linearly with the number of lamellar terminations. Degenerate microstructures and lamellar microstructures that have been mechanically deformed can show coarsening quite quickly<sup>13,58</sup> (in a few minutes at 540°C).<sup>57</sup> Significant changes in stable lamellar material will not be evident for many hours at temperatures near the melting point of the eutectic.<sup>56</sup>

Coarsening can be ignored in this work because of the relatively short times at high temperatures involved (1/2 hour at highest temperature/run). In any case, the change in microstructure was not significant enough to merit changing the ideal model microstructure.

## 2. Precipitation

A. D. Banchik and Alberto Bonfiglioli<sup>59</sup> have found through diffraction and small angle scattering of x-rays that the precipitation process common to other Al alloys<sup>60,61</sup> i.e., the precipitation sequence  $GP(1) \rightarrow GP(2) \rightarrow \theta' \rightarrow \theta$  can occur in the Al-CuAl<sub>2</sub> lamellar eutectic. The process is similar to that in metastable Cu-rich Al solid solutions, with the exception that since the  $\theta$  phase is already present in the adjacent lamellae, no  $\theta$  phase need be nucleated.<sup>62</sup> Banchik and Bonfiglioli<sup>59</sup> also cite evidence of age-hardening in the eutectic,<sup>3,10,63</sup> correlating the peak hardness times and temperatures with work in 4 w/o Cu-Al alloys.<sup>60</sup> Banchik and Bonfiglioli<sup>59</sup> have also published a scanning electron microscope photograph of  $\theta'$  precipitates in their typical Widmanstätten pattern in the Al phase of the lamellar eutectic.

For precipitation to occur in the Al phase in the Al-CuAl<sub>2</sub> directionally solidified eutectic, a supersaturation of Cu in the Al solid solution must be obtained by quenching the material. If the material is not quenched hard enough, the excess Cu solute will diffuse directly to the  $\theta$  phase lamellae. This is an explanation of why previous workers<sup>64</sup> may have missed finding precipitates in the Al phase. None of the specimens in this work were quenched, as all measurements were made in the as grown condition and relatively slow cooling rates in vacuum were employed. Therefore, it is concluded that precipitation is not a major consideration.

A related consideration is that the solubility of Cu in the Al solid solution varies with temperature. Thus the change in thickness of

the  $\theta$  lamellae from solidification to room temperature is  $\sim 10\%$ .<sup>64</sup> The shrinkage and expansion<sup>17</sup> of the  $\theta$  phase as the temperature increases and decreases has been ignored in this work.

#### D. EFFECTS OF MICROSTRUCTURE ON THERMAL EXPANSION

The effects on thermal expansion of dislocation, misorientation of the lamellae with respect to the ideal dilatometer axis, bending of the lamellae, and texture of the  $\theta$  phase are considered here.

The effect of dislocations is not accounted for in the elastic rule of mixtures. The coupling effect at the lamellar termination is not known, though it is known that the density of misfit dislocations increases with curvature, and is considerably greater than for the planar surface.<sup>16,17,20</sup>

The effect of changes in lamellar orientation with respect to ingot coordinates is of the form

$$\epsilon = |\cos\phi \vec{\epsilon}_1 - \sin\phi \vec{\epsilon}_2|$$

where for the ideal orientation  $\phi=0$ ,  $\vec{\epsilon}_1$  is the thermal expansion in the ideal direction, and  $\vec{\epsilon}_2$  is the thermal expansion in a direction orthogonal to the ideal direction. Hence if  $\phi$  is small,  $\epsilon \cong |\vec{\epsilon}_1|$  still. Of greater concern is the fact that one is forced to use an average lamellar orientation, so that

$$\epsilon = \frac{\int_{\text{specimen}} [(\cos^2\phi)\epsilon_1^2 + (\cos^2\psi)\epsilon_2^2 + (\cos^2\eta)\epsilon_3^2] dV}{\int_{\text{specimen}} dV}$$

where the axis of the dilatometer specimen is expressed as

$$\vec{a} = \cos\phi \frac{\vec{\epsilon}_1}{|\vec{\epsilon}_1|} + \cos\psi \frac{\vec{\epsilon}_2}{|\vec{\epsilon}_2|} + \cos\eta \frac{\vec{\epsilon}_3}{|\vec{\epsilon}_3|} \text{ and the ideal orientation is when } \phi = 0, \\ \psi = 90^\circ, \eta = 90^\circ.$$

The bending of the lamellae presents two other difficulties in approximating the real microstructure with the ideal microstructure assumed for the calculations. The first difficulty is finding an average normal of the lamellae to designate an orientation of the lamellae in ingot coordinates. The average inclination of the lamellae in a photograph may be difficult to ascertain because of the bending and defects present (though less so), especially in photographs of polished surfaces whose normals coincide with the growth direction where the number of defects and variance in inclination of the projection of the lamellae have been found to be greatest, and in photographs where the polished surface normals are close to the lamellae normals (defects and variance in orientation will be exaggerated). Once vectors have been assigned to these projections, the three sets of cross-products may be different because these vectors are taken from different parts but howbeit close parts of the ingot, and hence the orientation of the lamellae may be slightly different. Hence, the average of the three cross-products is used, or the best determined normal, usually that cross-product of vectors from the top and side of the ingot. For these reasons, the lamellae spacing formulae (Eq. (24)) may not be completely consistent when the two surfaces exchange roles.

The second effect is that bending of the lamellae violates the condition that the lamellar are planar in the ideal microstructure, but the effect should be small as far as the role of mixtures is concerned if the radius of curvature is much greater than the lamellar spacing, in which case the approximation of plane would still be valid.

The effects of the apparaent bending of the lamellae locally (Figure 13) should average out as above if the period and amplitude of the bending is not too great.

The effect of changing texture of the  $\theta$  phase can be treated similarly to the method described above with the analogous condition that the orientation of the  $\theta$  phase cannot change rapidly over the volume of the lamellae; the result would be an average value for the thermal expansion of the  $\theta$  phase to be used in the computations.

The relationship  $(111)_{Al} \parallel (121)_{\theta} \langle \bar{1}\bar{2}1 \rangle_{Al} \parallel \langle 12\bar{3} \rangle_{\theta}$  is not exact but only a low indice expression for the true relationship about this relationship. The interface relationship between the phases has been found to vary within the same specimen.<sup>16,20</sup> This variance can be as much as  $12^{\circ}$ .<sup>14</sup> Also the normal calculated by using the average projections of the lamellae as described earlier is not exact for reasons stated above. Since this variance is of the order of  $\pm 10^{\circ}$  depending on the ingot, the fact that the normal and the  $(111)_{Al}$  and  $(121)_{\theta}$  poles do not coincide on the stereographic projections is not surprising. However, the crystallographic relationship above has been taken as the average interface relationship for all the ingots, and has been so used in the calculations.

## VI. CONCLUSIONS

The thermal expansion of the directionally solidified Al-CuAl<sub>1</sub> eutectic decreases with increasing lamellar spacing for the range 1.4 to 7.5  $\mu\text{m}$ . This lamellar dependence is not accounted for by the rule of mixtures based on volume fractions. The thermal expansion is greatest in the growth direction, least in the transverse direction, and the thermal expansion normal to the lamellae is slightly greater than it is in the transverse direction. These results confirm that the CuAl<sub>2</sub> phase is anisotropic with regards to thermal expansion.

The most important implications of the results of this work is that the designer not only must take into account the fact that for high temperature applications the yield strength of the directionally solidified lamellar eutectic declines, but also that the dimensional tolerances will change due to the change in thermal expansion as coarsening proceeds.



## VII. ACKNOWLEDGEMENTS

I am sincerely grateful to Professor R. H. Bragg for his patience and guidance in helping to produce this report. I also thank Professors A. W. Searcy and V. F. Zackay for reviewing the text. Special thanks are due to S. Justi for helping with the directional solidification of the alloys and metallography, Lee Johnson for his attention and help while I was doing the metallography, and Professor R. M. Fulrath for helping identify and solve the problem of accounting for the deformation of the specimens. I want to show my appreciation for the technical assistance of the MMRD staff: Julian Patenaude, Duane Newhouse, Herb Riebe, and Ed Edwards for their help and cooperation in the machine shop; Brian Pope for preparing the master alloy and rewinding the furnace; Jack Wodei for help in maintaining the furnace instrumentation; Jim Severns and Glen Baum for keeping the dilatometer in working order; Gloria Pelatowski for the line drawings, and Carmen Hubbard for typing the manuscript.

This work was made possible by the U. S. Department of Energy through the auspices of the Lawrence Berkeley Laboratory, Materials and Molecular Research Division.

REFERENCES

1. R. W. Kraft, D. L. Albright (TMS-AIME 221, 95-102 (1961).
2. F. D. Lemkey, NASA CR-2778, Nov. 1973.
3. A. S. Yue, F. W. Crossman, A. E. Vidoz, M. I. Jacobsen, TMS-AIME 242, 2241 (1968).
4. R. W. Hertzberg, F. D. Lemkey, J. A. Ford, TMS-AIME 233, 342 (1965).
5. Michel Dupeaux, Francis Durand, Met. Trans 6A, 2143 (1975).
6. G. A. Chadwick, Acta Met. 24, 1137 (1976).
7. B. Cantor, G. A. Chadwick, J. Mat. Sci. 10, 578 (1975).
8. B. Cantor, G. J. May, G. A. Chadwick, J. Mat. Sci. 8, 830 (1973).
9. I. G. Davies, A. Hellawell, Phil. Mag. 19, 1285 (1969).
10. H. R. Bertorello, H. Biloni, Met. Trans. 3, 73 (1972).
11. R. G. McKay, M. Sc. Thesis, University of Queensland (1974).
12. A. Pattnaik, A. Lawley, Met. Trans. 2, 1529 (1971).
13. M. W. A. Bright, D. M. R. Taplin, H. W. Kerr, Trans. ASME 97, Ser. H, 1-9 (J. of Eng. & Mat. Tech., Jan. 1975).
14. I. G. Davies, A. Hellawell, Phil. Mag. 19, 1255 (1969).
15. I. G. Davies, A. Hellawell, Phil. Mag. 19, 1299 (1969).
16. G. Garmong, C. G. Rhodes, Met. Trans. 5A, 2507 (1974).
17. G. Garmong, C. G. Rhodes, Acta Met. 22, 1373 (1974).
18. R. W. Kraft, A. L. Albright, TMS-AIME 224, 1176-1184 (1962).
19. R. W. Kraft, TMS-AIME 224, 65-74 (1962).
20. G. C. Weatherly, Met. Sci. J. 2, 25-27 (1968).

21. R. Bonnet, F. Durand, Conf. on In Situ Composites Vol. 1, p. 209 (1972).
22. K. A. Jackson, J. D. Hunt, TMS-AIME 236, 1129 (1966).
23. C. Zener, TMS-AIME 167, 550 (1946).
24. J. N. Clark, R. Elliott, Met. Trans. 7A, 1197 (1976).
25. G. A. Chadwick, J. Inst. Met. 91, 169 (1963).
26. R. M. Jordan, J. D. Hunt, Met. Trans. 2, 3401 (1971).
27. D. J. S. Cooksey, D. Munson, M. P. W. Wilkinson, A. Hellawell, Phil. Mag. 10, 745 (1964).
28. R. M. Jordan, J. D. Hunt, Met. Trans. 3, 1385 (1972).
29. J. D. Hunt, J. P. Chilton, J. Inst. Met. 93, (1963-4).
30. A. S. Yue, Proceeding of an International Conference on Crystal Growth, p. 197 (1967).
31. W. A. Tiller, K. A. Jackson, J. W. Rutter, B. Chalmers, Acta Met. 428-37 (1953).
32. F. R. Mollard, M. C. Flemings, TMS-AIME 236, 1526 (1967).
33. Zvi Hashin, "Elasticity of Ceramic Systems" Ceramic Microstructures, Richard M. Fulrath, Joseph A. Pask, ed., John Wiley & Sons, N. Y. Ch. 14, p. 313 (1968).
34. G. Garmon, Met. Trans. 5, 2191 (1974).
35. Thermophysical Properties of High Temperature Solid Materials, Y. S. Touloukian, ed., (TPRC) Vol. 1, 17-18 (1967).
36. Aluminum, Vol. 1., Properties, Physical Metallurgy and Phase Diagrams, Kent R. Van Horn, ed., ASM, p. 4 (1967).
37. D. M. Rabkin, V. R. Ryabov, A. V. Losovskaya, V. A. Dorzhenko, Sov. Powder Met. Ceram. 8, 695 (1970).

38. I. G. Daives, D. Phil. Thesis, Oxford p. 123 (1969).
39. B. Paul, TMS-AIME 218, 36 (1960).
40. R. Hill, J. Mech. Phys. Sol. 12, 199-213 (1964).
41. George E. Mase, Schaum's Outline of Theory and Problems of Continuum Mechanics, McGraw-Hill, p. 149 (1970).
42. F. Lazlo, J. Iron Steel Inst. 148, 173-99) (1943).
43. C. S. Barrett, Structure of Metals, McGraw-Hill, New York, p. 455 (1943).
44. E. M. Savitskii in Mechanical Properties in Intermetallic Compounds, J. H. Westbrook, ed., John Wiley & Sons, N. Y. p. 91, 94 (1960).
45. R. F. Wilde, N. J. Grant (ASTM Proc. 57, 917-928 (1957).
46. S. Justi, R. H. Bragg, LBL 4560 Preprint, (1975).
47. J. D. Hunt, K. A. Jackson, TMS-AIME 236, 843 (1966).
48. A. S. Yue, TMS-AIME 224, 1010 (1962).
49. L. Valero, M. S. Thesis, University of California, Berkeley, (1977).
50. ASTM E228-71.
51. G. Garmong, Met. Trans. 5, 2183 (1974).
52. G. Garmong, C. G. Rhodes, Conf. on In Situ Composites, Vol. 1, p. 251, Lakeville, Conn. (1972).
53. Y. G. Nakagawa, G. C. Weatherly, E. Ho, Trans. Jap. Inst. Met. 15, 115 (1974).
54. W. W. Mullins, J. Appl. Phys. 30, 77 (1960).
55. W. W. Mullins, J. Appl. Phys. 28, 333 (1957).
56. L. D. Graham, R. W. Kraft, TMS-AIME 236, 94 (1966).

57. E. Ho, G. C. Weatherly, Acta Met. 23, 1451 (1975).
58. B. R. Butcher, G. C. Weatherly, H. R. Petit, Met. Sci. 3, 7-13 (1969).
59. A. D. Banchik, Alberto Bonfiglioli, Phil. Mag. 30, 691-703 (1974).
60. J. H. Silcock, T. J. Heal, H. I. Hardy, J. Inst. Met. 82, 239 (1953-4).
61. Precipitation from Solid Solution, J. B. Newkirk ed., ASM (1959).
62. C. Laird, H. I. Aaronson, Acta Met. 14, 171 (1966).
63. H. W. Crossman, A. S. Yue, A. E. Vidoz, TMS-AIME 245, 393 (1969).
64. D. R. Spalding, R. E. Villagrana, G. A. Chadwick, Phil. Mag. 20, 471 (1969).
65. Thermophysical Properties of High Temperature Solid Materials, Y. S. Tsvetkovskiy, ed., (TPRC) Vol. 1, 462-3 (1967).
66. Handbook of Physics and Chemistry, Robert C. Weast, ed., 53rd ed., CRC, Cleveland, F-59 (1972).
67. S. Justi, to be published.

LIST OF TABLES

- I. Mean Thermal Expansion Coefficients of Al and  $\text{CuAl}_2$   
(literature).
- II. Calculated Composite Mean Thermal Expansion.
- III. Summary of lamellar spacings and orientations.
- IV. Qualitative Raw Data Results (grouping together of cycles).
- V. Thermal Expansion of the  $\text{CuAl}_2$ -Al Directionally Solidified  
Eutectic.

Table I. Mean thermal expansion coefficients of  
Al and  $\text{CuAl}_2$  (literature).

Temp $^{\circ}\text{C}$	$\alpha_{\text{Al}}$ $\times 10^{-6} \text{ }^{\circ}\text{C}^{-1}$	$\alpha_{\text{long}\theta}$ $\times 10^{-6} \text{ }^{\circ}\text{C}^{-1}$	$\alpha_{\text{trans}\theta}$ $\times 10^{-6} \text{ }^{\circ}\text{C}^{-1}$	$\alpha_{\text{vertical}\theta}$ $\times 10^{-6} \text{ }^{\circ}\text{C}^{-1}$
100	23.8	21.0	15.3	17.3
200	24.5	21.3	15.5	17.5
300	25.4	21.6	15.7	17.8
400	26.5	21.7	15.8	17.9
500	27.1	22.7	16.5	18.7

Table II. Calculated composite mean thermal expansion.

$^{\circ}\text{C}$	Longitudinal		Vertical		Transverse	
	$\overline{\alpha}_m$		$\overline{\alpha}_m$		$\overline{\alpha}_m$	
	$\frac{\Delta L}{L} \%$	$10^{-6} \text{ } ^{\circ}\text{C}^{-1}$	$\frac{\Delta L}{L} \%$	$10^{-6} \text{ } ^{\circ}\text{C}^{-1}$	$\frac{\Delta L}{L} \%$	$10^{-6} \text{ } ^{\circ}\text{C}^{-1}$
100	.178	22.3	.162	20.3	.154	19.2
200	.410	22.8	.374	20.8	.353	19.6
300	.652	23.3	.596	21.3	.563	20.1
400	.908	23.9	.832	21.9	.787	20.7
500	1.186	24.7	1.085	22.6	1.022	21.3



Table III. Summary of lamellar spacings and orientations.

$\frac{R}{\text{cm/sec} \times 10^{-4}}$	$\lambda$ $\mu\text{m}$	$\hat{n}$ ingot coordinates
0.958	7.5	$-.041 \hat{i} + .073 \hat{j} + .997 \hat{k}$
3.97	3.5	$.003 \hat{i} + .347 \hat{j} + .938 \hat{k}$
8.33	2.6	$-.177 \hat{i} + .304 \hat{j} + .935 \hat{k}$
17.5	1.8	$-.077 \hat{i} + .988 \hat{j} - .130 \hat{k}$
82.2	1.4	polycrystalline

$\hat{i}$  - growth direction

$\hat{j}$  - vp (from horizontal)

$\hat{k}$  - transverse (right hand coordinate system)

Table IV. Qualitative raw data results (grouping together cycles).

$\lambda (\mu\text{m})$	7.5	3.5	2.6	1.8	1.9
direction					
longitudinal	mod. tight	tight	loose	loose	mod. tight
vertical	mod. tight	loose	tight	loose	mod. tight
transverse	mod. tight	loose	loose	very loose	loose

Table V. Thermal Expansion of the CuAl<sub>2</sub>-Al directionally solidified eutectic.

°C		Longitudinal		Vertical		Transverse	
		$\frac{\Delta L}{L} \%$	$\frac{\alpha_m}{\times 10^{-6} \text{ } ^\circ\text{C}^{-1}}$	$\frac{\Delta L}{L} \%$	$\frac{\alpha_m}{\times 10^{-6} \text{ } ^\circ\text{C}^{-1}}$	$\frac{\Delta L}{L} \%$	$\frac{\alpha_m}{\times 10^{-6} \text{ } ^\circ\text{C}^{-1}}$
100	$\lambda = 7.5 \text{ } \mu\text{m}$	.157±.009	19.6±3.1	.140±.012	17.5±1.9	.116±.011	14.5±1.7
200		.365±.017	20.3±1.2	.320±.020	17.8±1.3	.274±.023	15.8±1.4
300		.578±.026	20.6±1.1	.503±.027	18.0±1.1	.438±.032	15.6±1.3
400		.786±.035	20.7±1.0	.689±.035	18.1±1.1	.609±.041	16.0±1.2
500		1.016±.046	21.2±1.0	.861±.043	17.9±1.0	.813±.049	16.9±1.1
100	$\lambda = 3.5 \text{ } \mu\text{m}$	.169±.006	21.1±1.3	.154±.013	19.3±1.9	.140±.009	18.4±1.1
200		.387±.013	21.5±1.0	.339±.024	18.8±1.4	.331±.016	18.4±1.1
300		.607±.019	21.6±0.8	.551±.036	19.7±1.4	.526±.024	18.8±1.0
400		.839±.025	22.1±0.8	.772±.048	20.3±1.4	.758±.033	20.0±1.0
500		1.109±.032	23.1±0.8	1.004±.063	20.9±1.4	1.092±.041	21.7±0.9
100	$\lambda = 2.6 \text{ } \mu\text{m}$	.185±.015	23.1±2.5	.168±.007	21.0±1.4	.157±.008	19.6±1.5
200		.426±.016	23.7±1.0	.380±.008	21.1±0.7	.349±.020	18.8±1.3
300		.683±.020	24.4±0.8	.597±.010	21.3±0.5	.547±.038	19.5±1.5
400		.982±.024	25.8±0.8	.831±.011	21.9±0.4	.767±.059	20.2±1.5
500		1.328±.035	27.7±0.8	1.079±.012	22.5±0.3	1.038±.065	21.6±1.4

(continued)

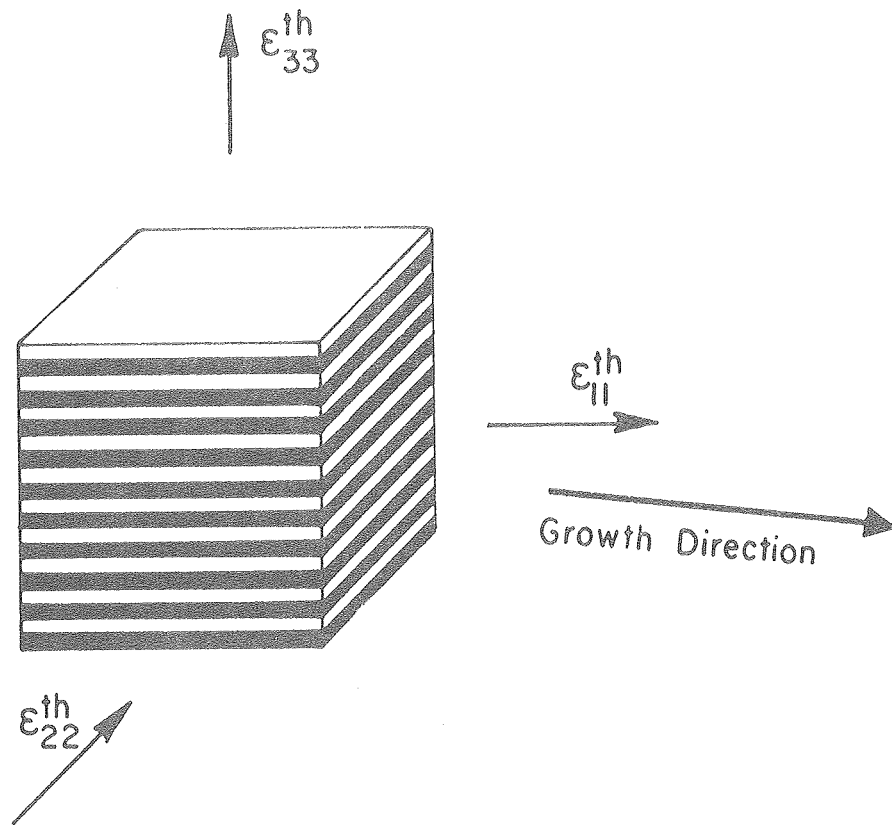
(Table V. (Continued))

$\lambda$	$\text{°C}$	Longitudinal		Vertical		Transverse	
		$\frac{\Delta L}{L} \%$	$\frac{\alpha_m}{\times 10^{-6} \text{ °C}^{-1}}$	$\frac{\Delta L}{L} \%$	$\frac{\alpha_m}{\times 10^{-6} \text{ °C}^{-1}}$	$\frac{\Delta L}{L} \%$	$\frac{\alpha_m}{\times 10^{-6} \text{ °C}^{-1}}$
$\lambda = 1.8 \text{ } \mu\text{m}$	100	.177 $\pm$ .009	22.1 $\pm$ 1.7	.164 $\pm$ .008	20.5 $\pm$ 1.5	.150 $\pm$ .008	18.8 $\pm$ 1.5
	200	.451 $\pm$ .023	25.1 $\pm$ 1.6	.369 $\pm$ .018	20.5 $\pm$ 1.2	.341 $\pm$ .016	18.9 $\pm$ 1.1
	300	.747 $\pm$ .031	26.7 $\pm$ 1.3	.585 $\pm$ .028	20.9 $\pm$ 1.1	.542 $\pm$ .029	19.4 $\pm$ 1.0
	400	1.075 $\pm$ .042	28.3 $\pm$ 1.3	.845 $\pm$ .037	22.2 $\pm$ 1.1	.731 $\pm$ .082	19.2 $\pm$ 0.9
	500	1.422 $\pm$ .052	29.6 $\pm$ 1.2	1.134 $\pm$ .048	23.6 $\pm$ 1.1	.941 $\pm$ .041	19.6 $\pm$ 0.9
$\lambda = 1.4 \text{ } \mu\text{m}$	100	.162 $\pm$ .011	20.3 $\pm$ 1.9	.156 $\pm$ .016	19.5 $\pm$ 2.5	.167 $\pm$ .009	20.9 $\pm$ 1.6
	200	.396 $\pm$ .018	22.0 $\pm$ 1.2	.350 $\pm$ .028	19.4 $\pm$ 1.8	.385 $\pm$ .013	21.4 $\pm$ 1.0
	300	.642 $\pm$ .023	22.9 $\pm$ 1.0	.557 $\pm$ .041	19.9 $\pm$ 1.6	.622 $\pm$ .019	22.2 $\pm$ 0.8
	400	.939 $\pm$ .032	25.0 $\pm$ 1.0	.814 $\pm$ .057	21.4 $\pm$ 1.5	.892 $\pm$ .026	23.5 $\pm$ 0.8
	500	1.209 $\pm$ .038	25.2 $\pm$ 0.9	1.088 $\pm$ .069	22.7 $\pm$ 1.5	1.181 $\pm$ .032	24.6 $\pm$ 0.8

FIGURE CAPTIONS

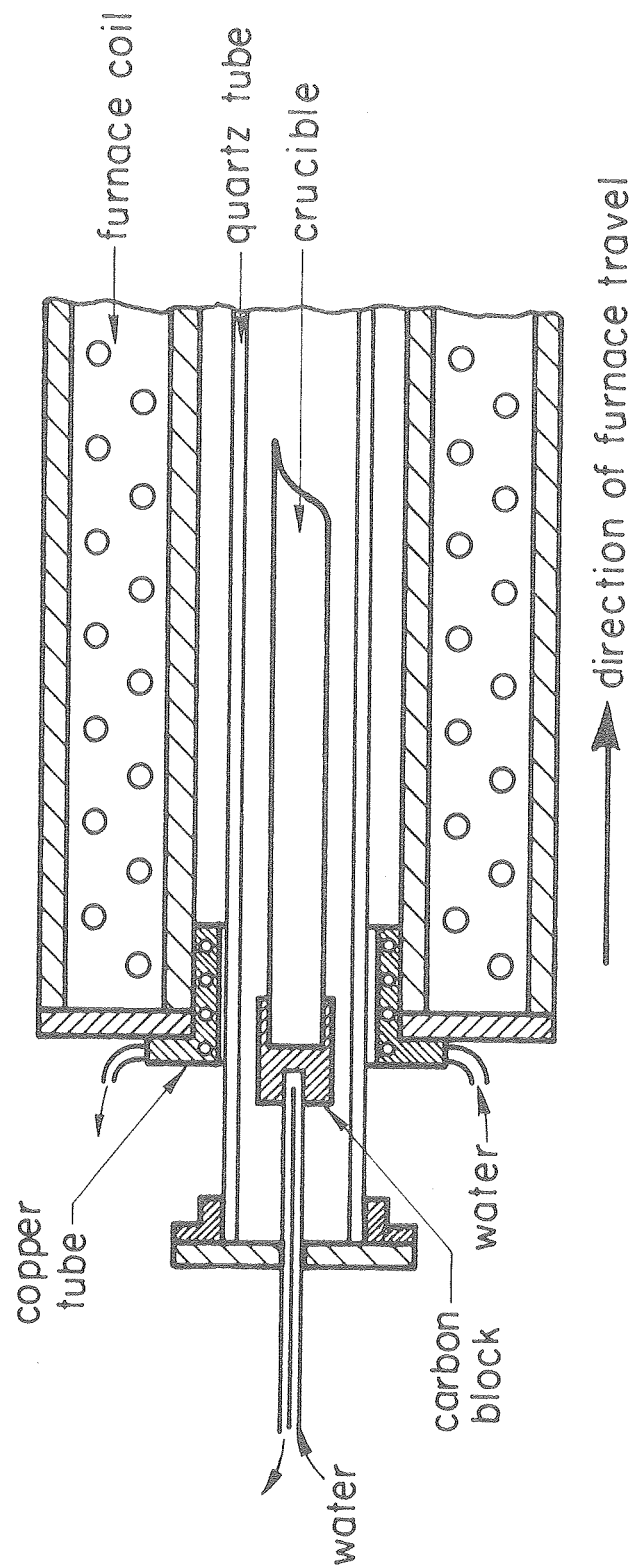
- Figure 1. Ideal microstructure.
- Figure 2. Solidification apparatus schematic (furnace).
- Figure 3. Detailed furnace schematic.
- Figure 4.  $\lambda^2$  vs. R.
- Figure 5. Sketch of macrostructure,  $\lambda = 7.5 \mu\text{m}$ .
- Figure 6. Sketch of macrostructure,  $\lambda = 3.5 \mu\text{m}$ .
- Figure 7. Sketch of macrostructure,  $\lambda = 2.6 \mu\text{m}$ .
- Figure 8. Sketch of macrostructure,  $\lambda = 1.8 \mu\text{m}$ .
- Figure 9. Sketch of macrostructure,  $\lambda = 1.4 \mu\text{m}$ .
- Figure 10. Micrograph of ideal microstructure,  $\lambda = 3.5 \mu\text{m}$ .  
side projection.
- Figure 11. Micrograph of dislocations  $\lambda = 2.6 \mu\text{m}$ ,  
transverse projection.
- Figure 12. Micrograph of shifting lamellae orientation.
- Figure 13. Micrograph of surface near lamellae normal,  $\lambda = 3.5 \mu\text{m}$ ,  
vertical projection.
- Figure 14A. (top half) Polycrystalline eutectic micrograph,  
 $\lambda = 1.4 \mu\text{m}$ , top projection.
- Figure 14B. (bottom half) Polycrystalline eutectic micrograph  
 $\lambda = 1.4 \mu\text{m}$ , transverse projection.
- Figure 15. Laue transmission photograph,  $\lambda = 7.5 \mu\text{m}$ ,  $(111)_{\text{Al}}$  orientation evident by 3-fold symmetry of streaks at center.

- Figure 16. Stereographic projection of transmission Laue photograph,  
 $\lambda = 7.5 \text{ } \mu\text{m}$ .
- Figure 17. Stereographic projection of transmission Laue photograph,  
 $\lambda = 3.5 \text{ } \mu\text{m}$ .
- Figure 18. Stereographic projection of transmission Laue photograph,  
 $\lambda = 2.6 \text{ } \mu\text{m}$ .
- Figure 19. Stereographic projection of transmission Laue photograph,  
 $\lambda = 1.8 \text{ } \mu\text{m}$ .
- Figure 20. Two surface lamellar spacing determination, general case.
- Figure 21. Machining of parallelepiped along dilatometer specimen  
axis.
- Figure 22. Specimen chamber of Theta IIIR dilatometer.
- Figure 23. Section of raw thermal expansion data chart recording.
- Figure 24. Determination of correction function. (Cu standard)
- Figure 25. Typical raw thermal expansion data.
- Figure 26. Thermal expansion for  $\lambda = 7.5 \text{ } \mu\text{m}$ .
- Figure 27. Thermal expansion for  $\lambda = 3.5 \text{ } \mu\text{m}$ .
- Figure 28. Thermal expansion for  $\lambda = 2.6 \text{ } \mu\text{m}$ .
- Figure 29. Thermal expansion for  $\lambda = 1.8 \text{ } \mu\text{m}$ .
- Figure 30. Thermal expansion for  $\lambda = 1.4 \text{ } \mu\text{m}$  (polycrystalline).
- Figure 31. Thermal expansion for the longitudinal direction.
- Figure 32. Thermal expansion for the vertical direction.
- Figure 33. Thermal expansion for the transverse direction.
- Figure 34. Calculated thermal expansion.



XBL 773-5200

Figure 1



XBL7512-9251

Figure 2



Figure 3

INDEX

- 1 - Quartz tube with crucible (C).
- 2 - Copper tube.
- 3 - Support of quartz tube (copper).
- 4 - Copper end disc with O-seal ring and thermocouple passage.
- 5 - Aluminum support.
- 6 - Water colling system.
- 7 - Moving furnace, front and end face: asbestos, laberal side:  
aluminum sheet, Marshall furnace, Max. AMP = 14.7.
- 8 - Track.
- 9 - Switch-end of course.
- 10 - Adjustable rods.
- 11 - Stainless steel wire for mechanical transmission.
- 12 - Drums (D=21).
- 13 - Scale.
- 14 - Pointer.
- 15 - Indicator of pressure on line.
- 16 - Indicator of pressure after regulator.
- 17 - Regulator.
- 18 - Indicator of pressure on tank.
- 19 - Flowmeter.

Figure 3 Index (continued)

- 20 - Valve of argon tank.
- 21 - Argon tank.
- 22 - Pulley  $P_1$ .
- 23 - Bear box.
- 24 - Electrical motor shaft.

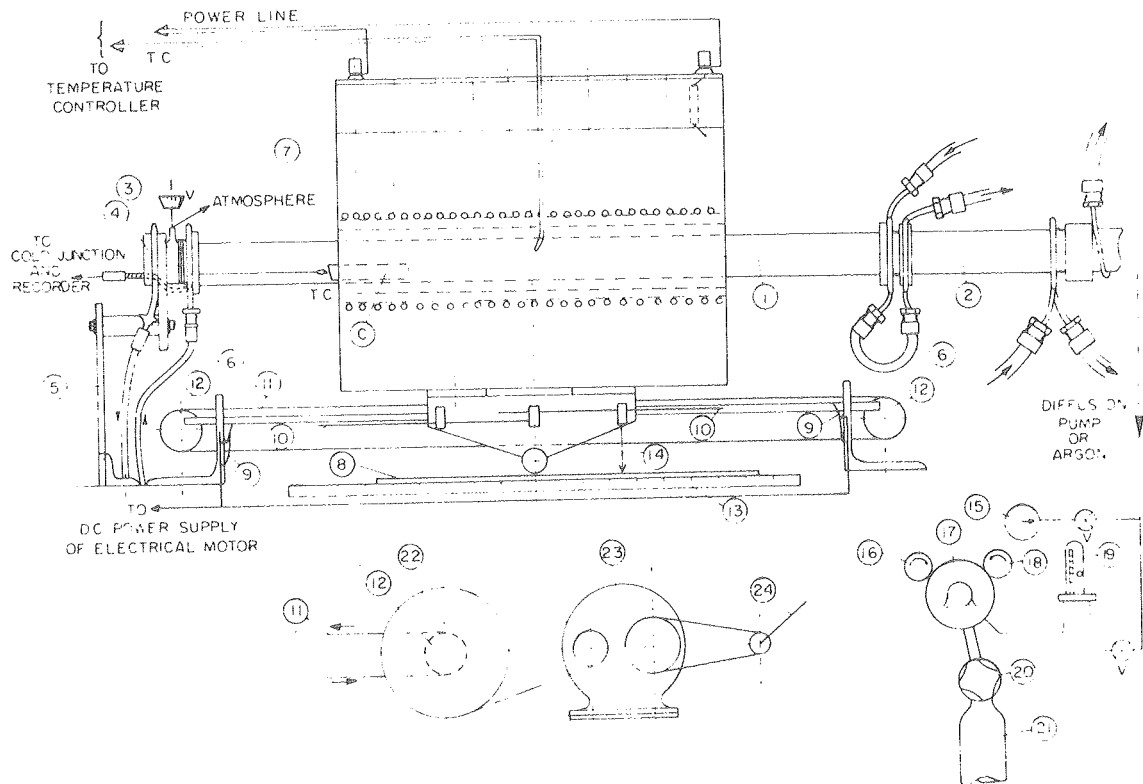
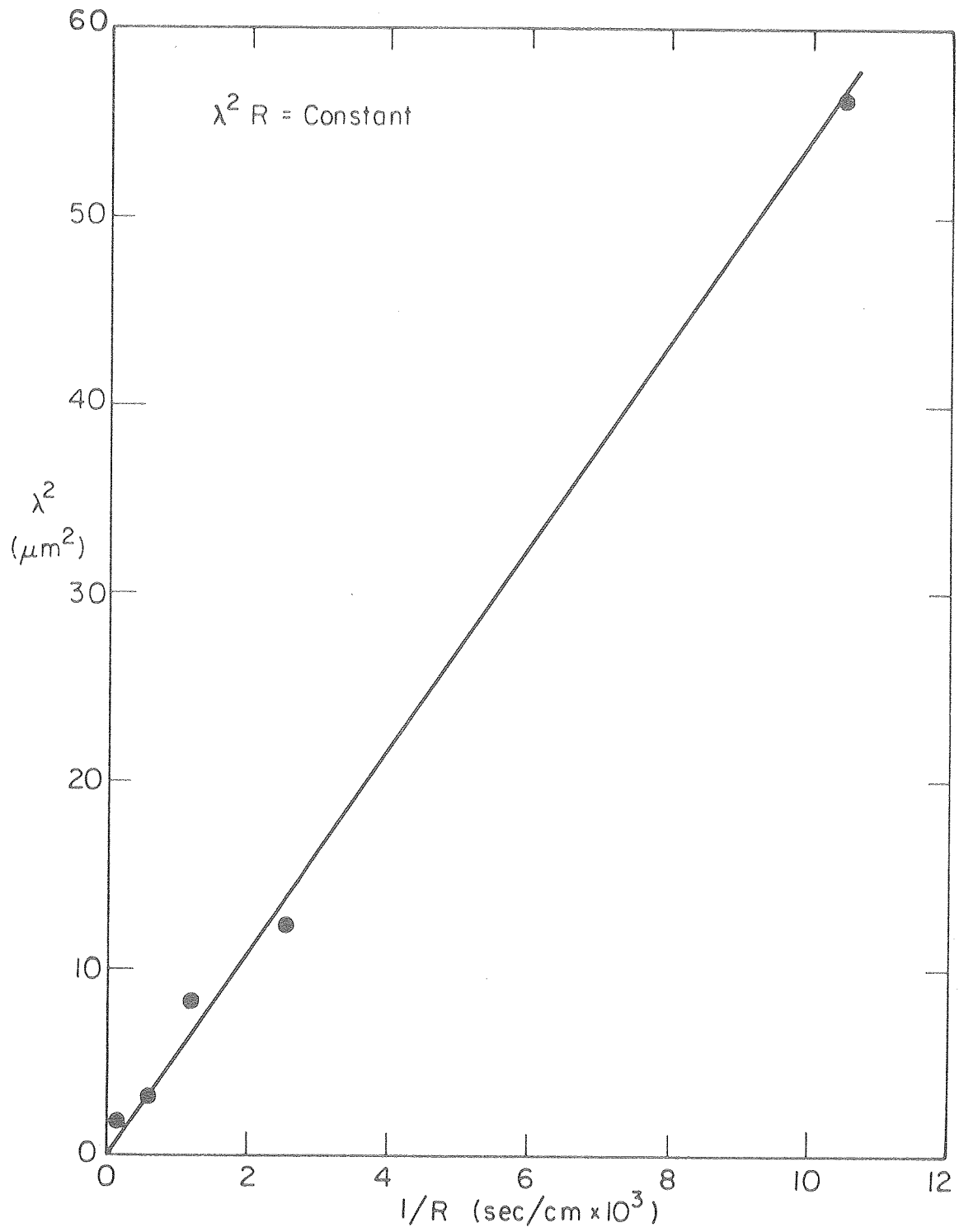


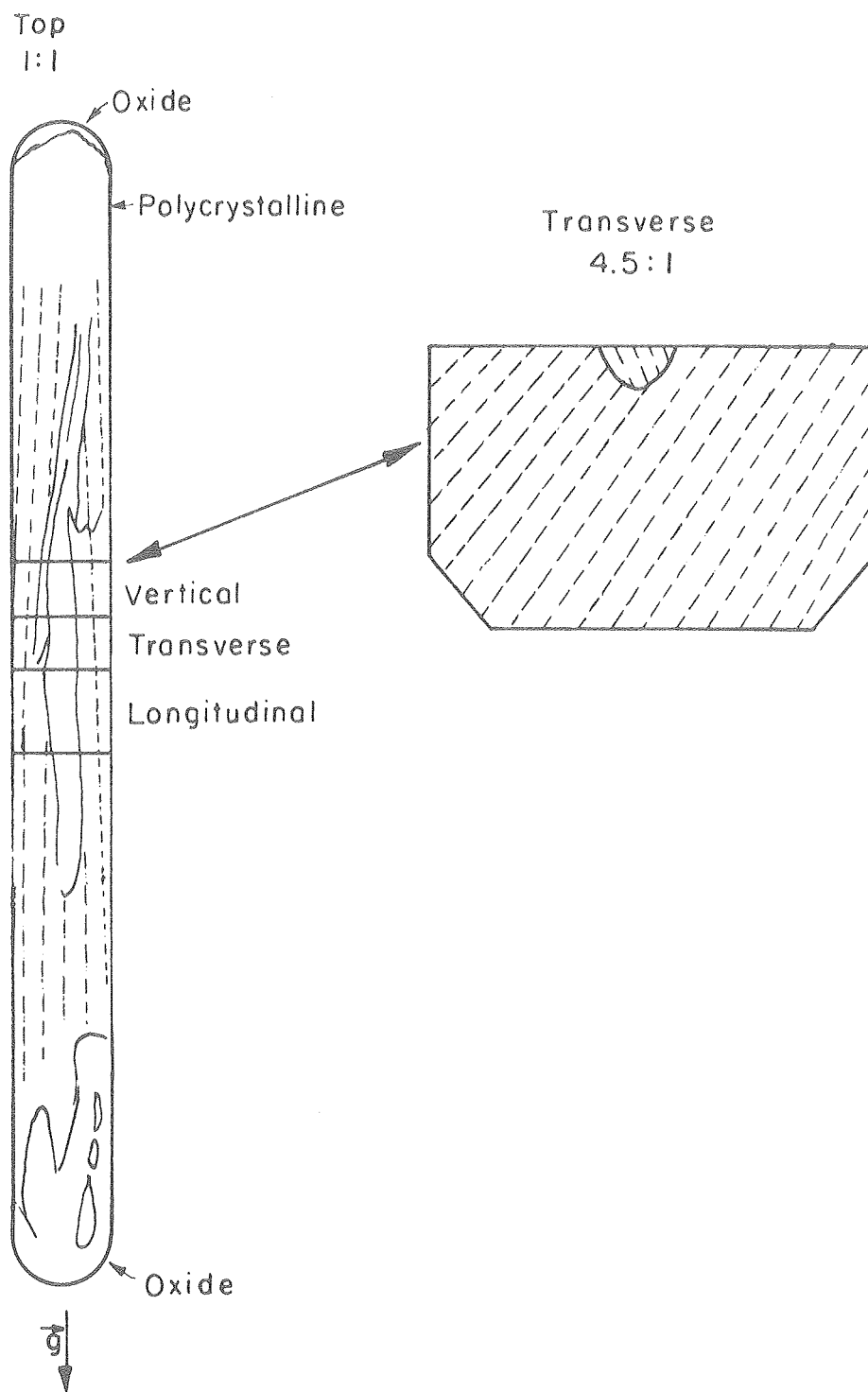
Figure 3



XBL 784 - 4829

Figure 4

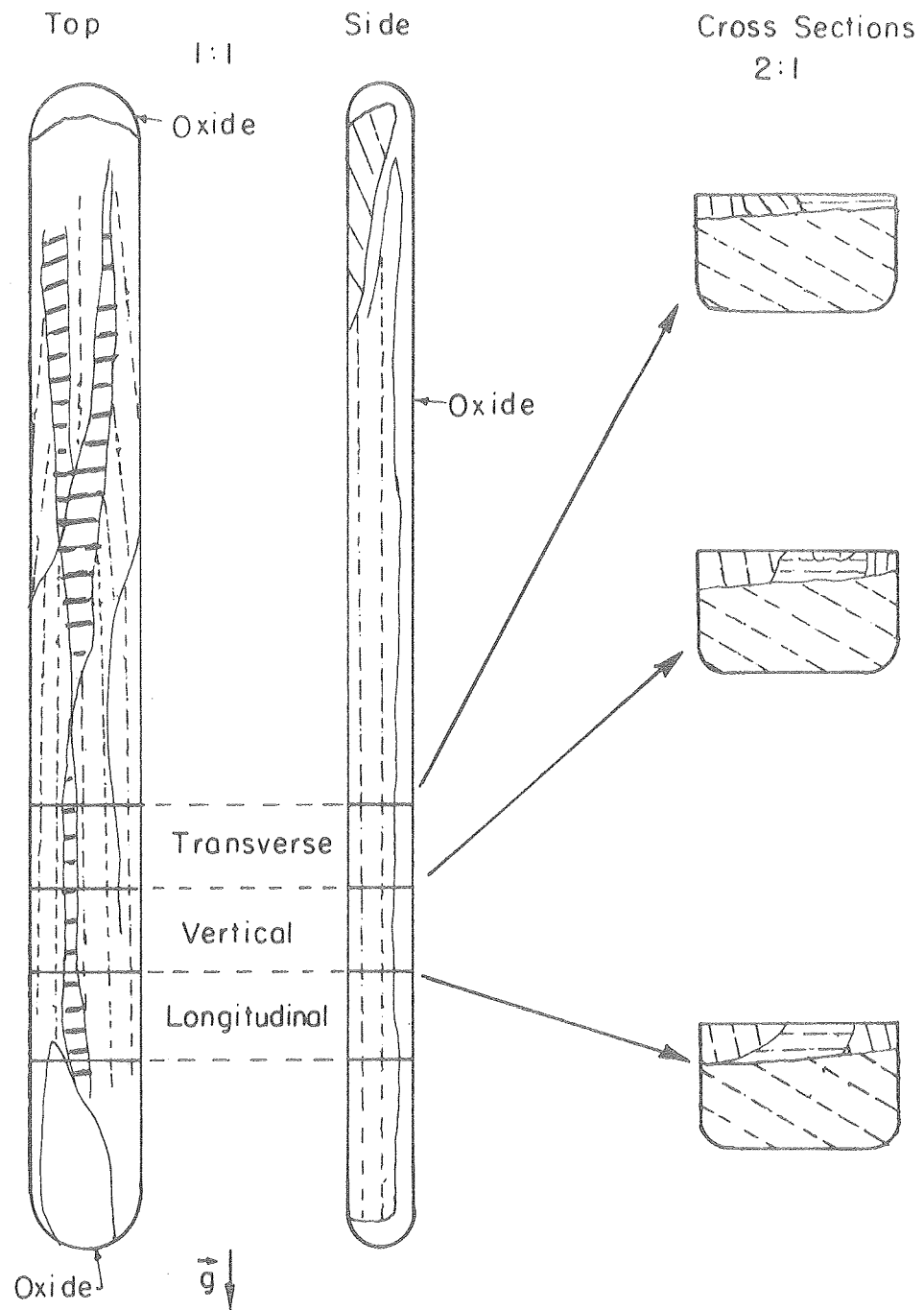
$$\lambda = 7.5 \mu\text{m}$$



XBL 783-4766

Figure 5

$\lambda = 3.5 \mu\text{m}$



XBL783-4767

Figure 6



Figure 7

$$\lambda = 1.8 \mu m$$

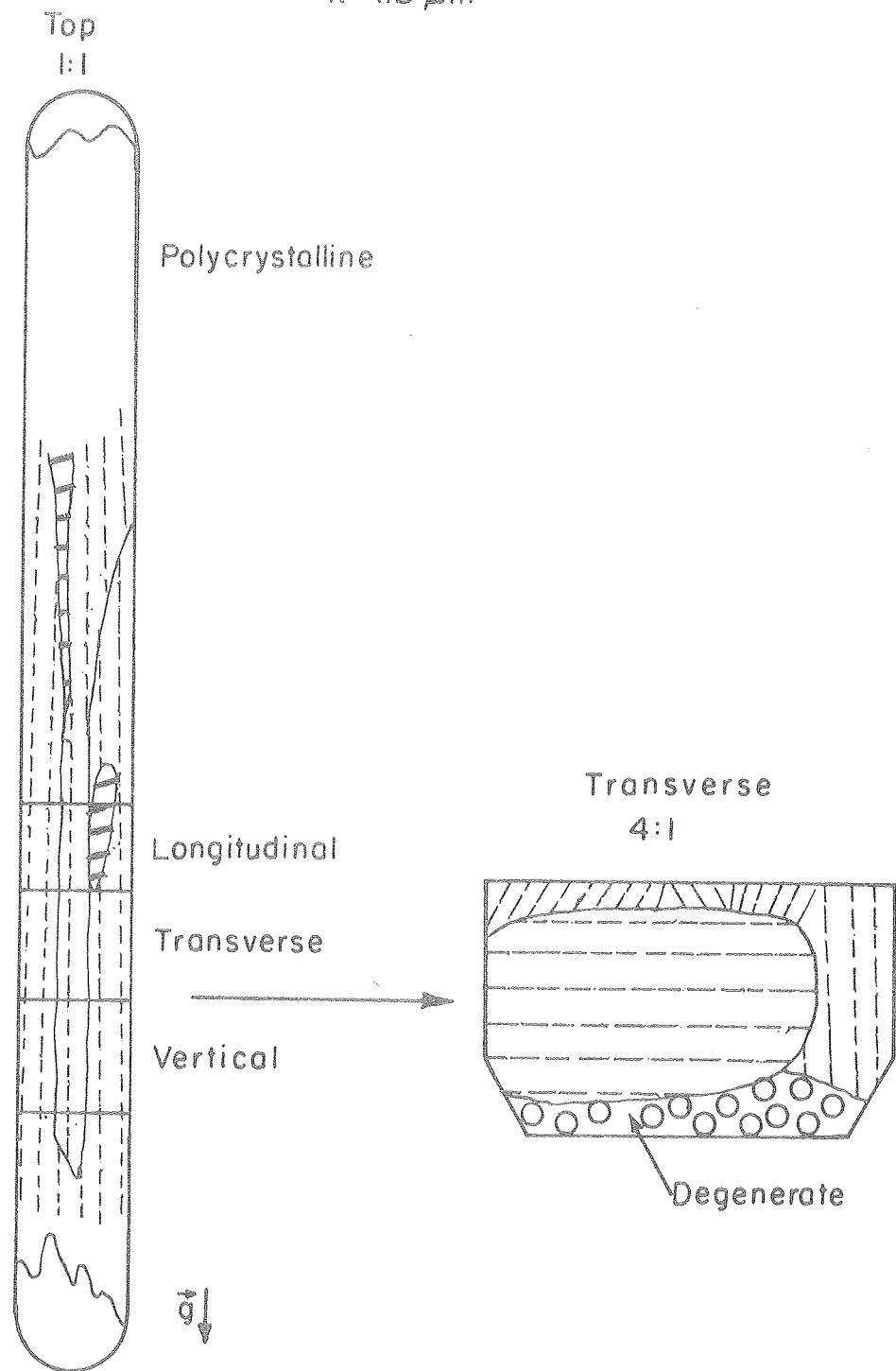
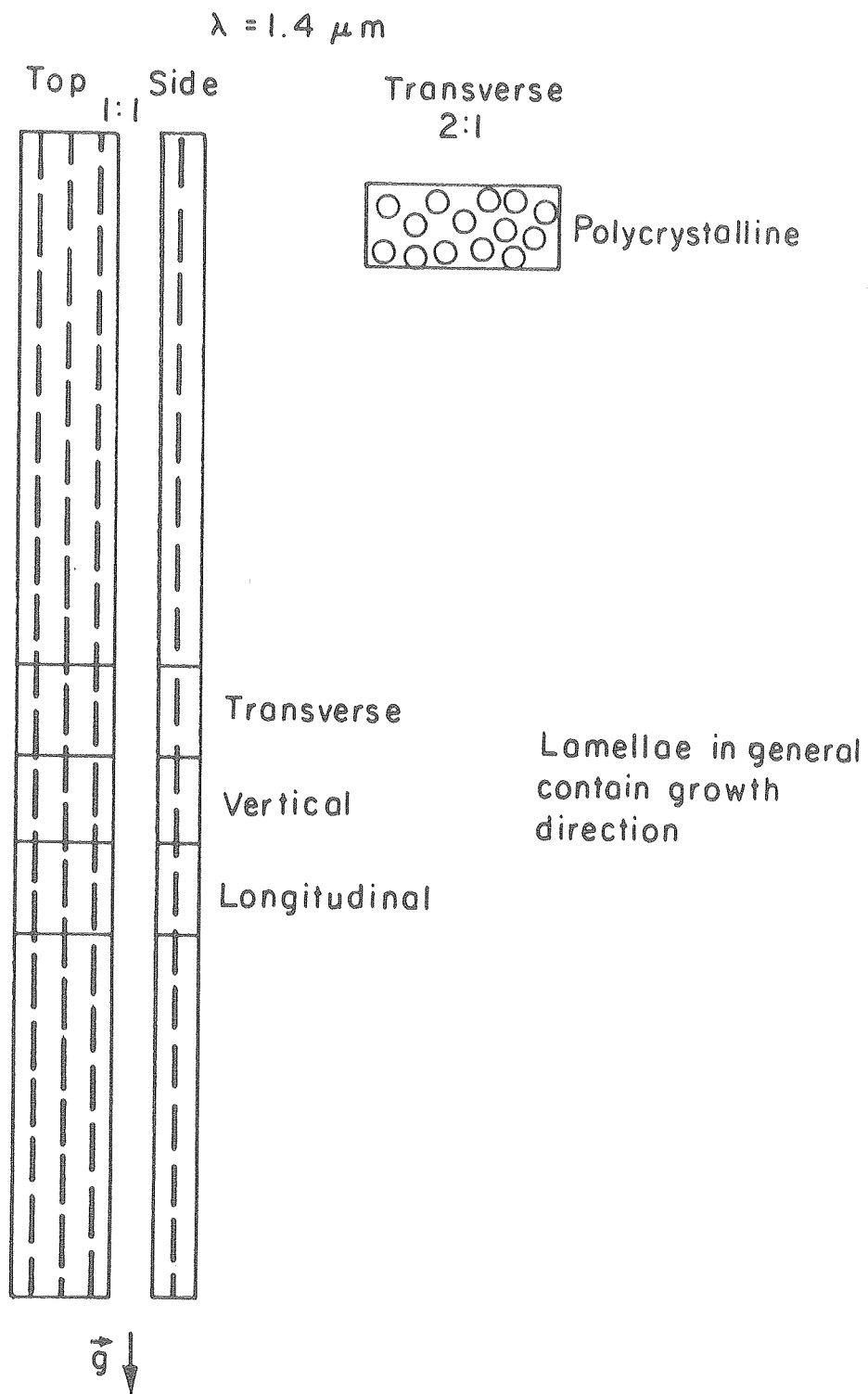


Figure 8

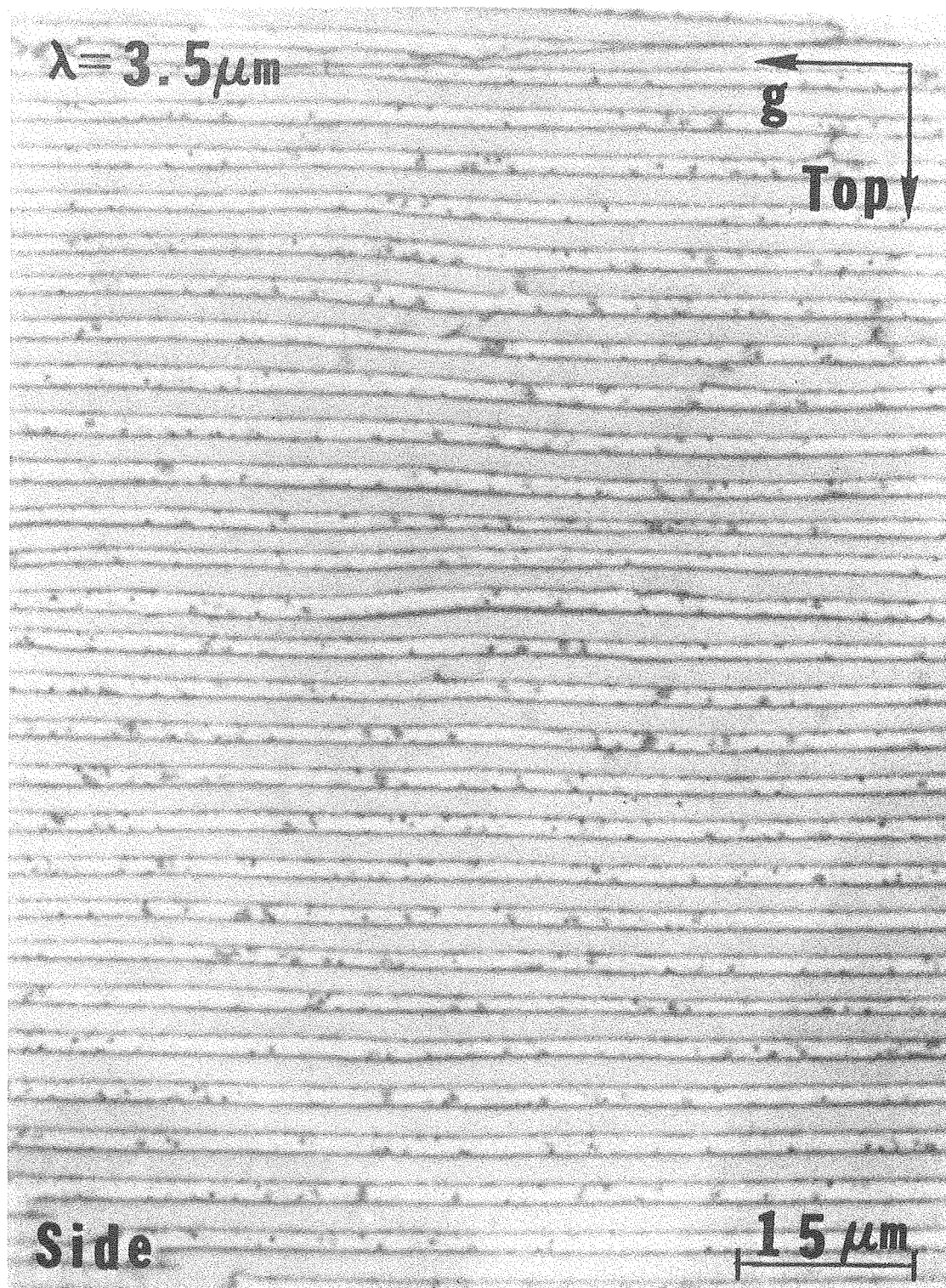
XBL783-4769





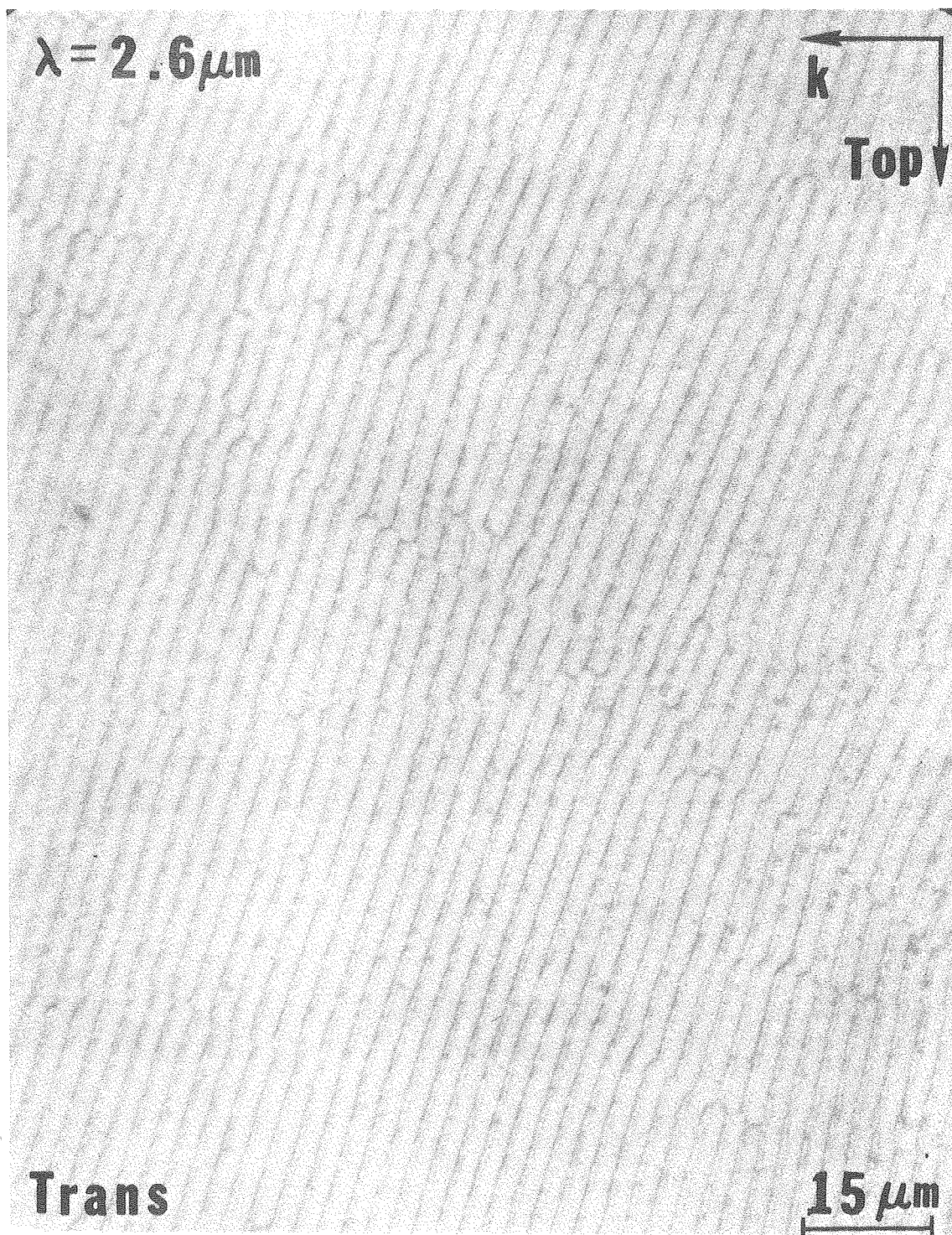
XBL 783-4770

Figure 9



XBB 784-4433

Figure 10



XBB 784-4431

Figure 11

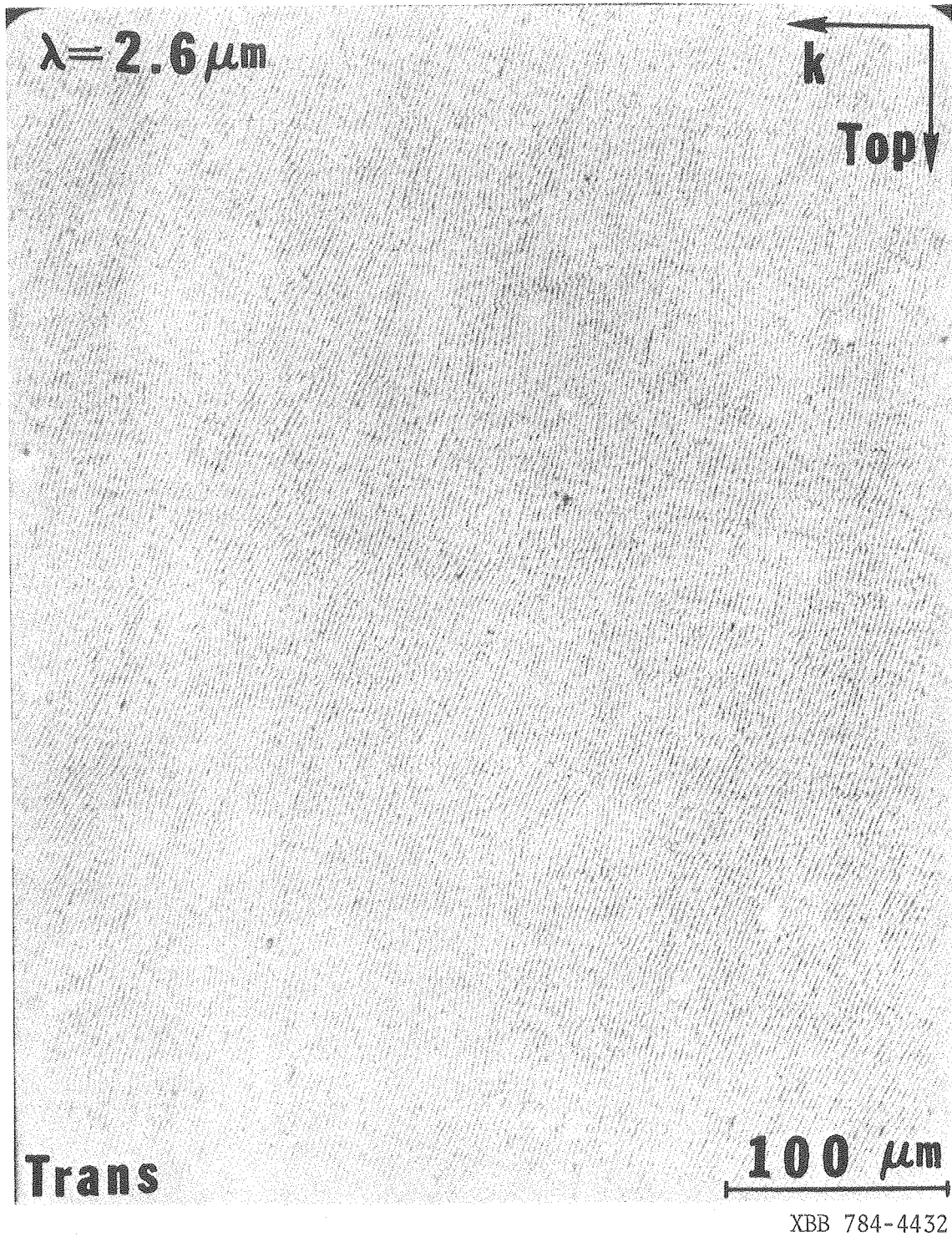


Figure 12



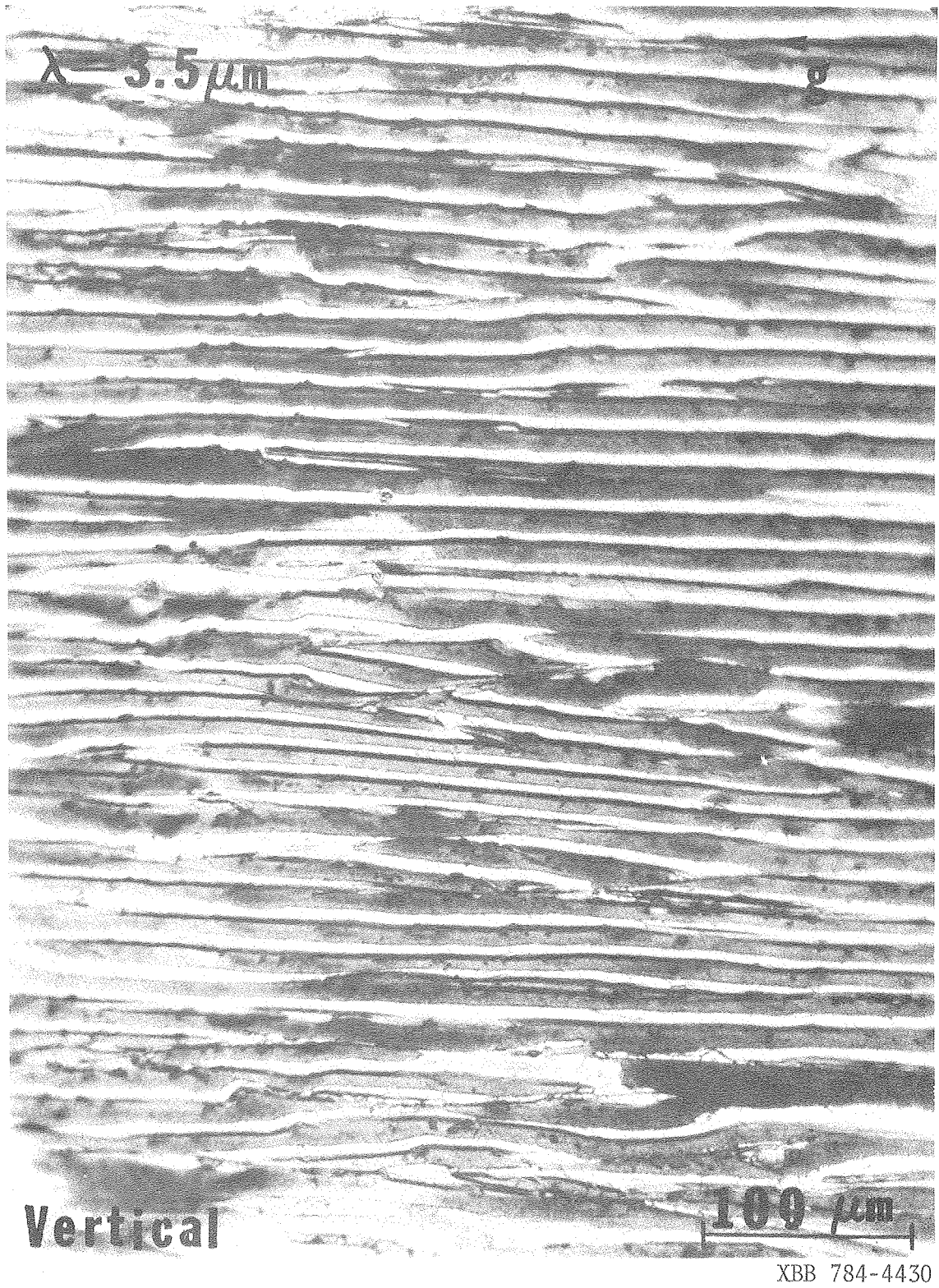


Figure 13

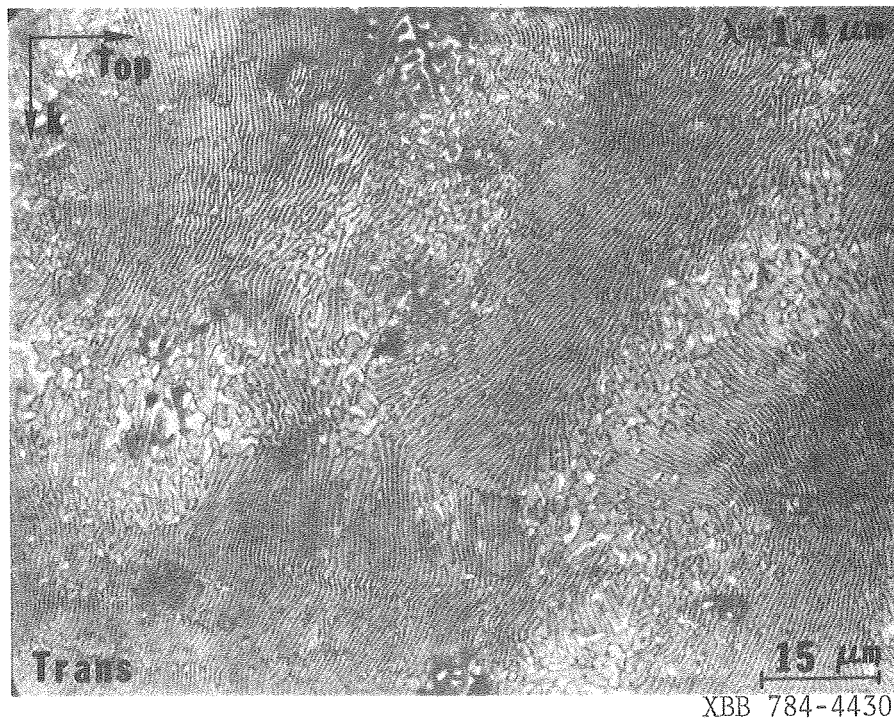
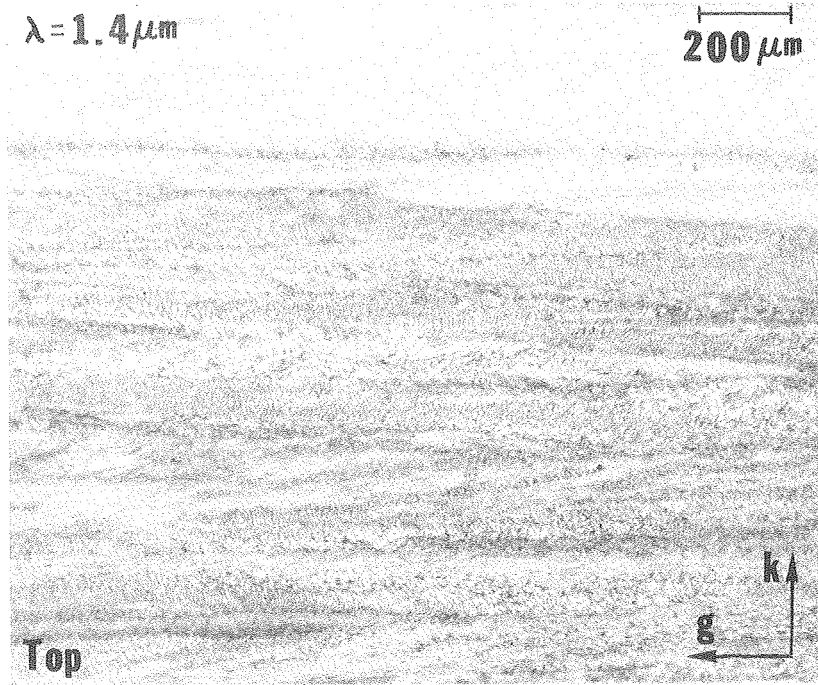
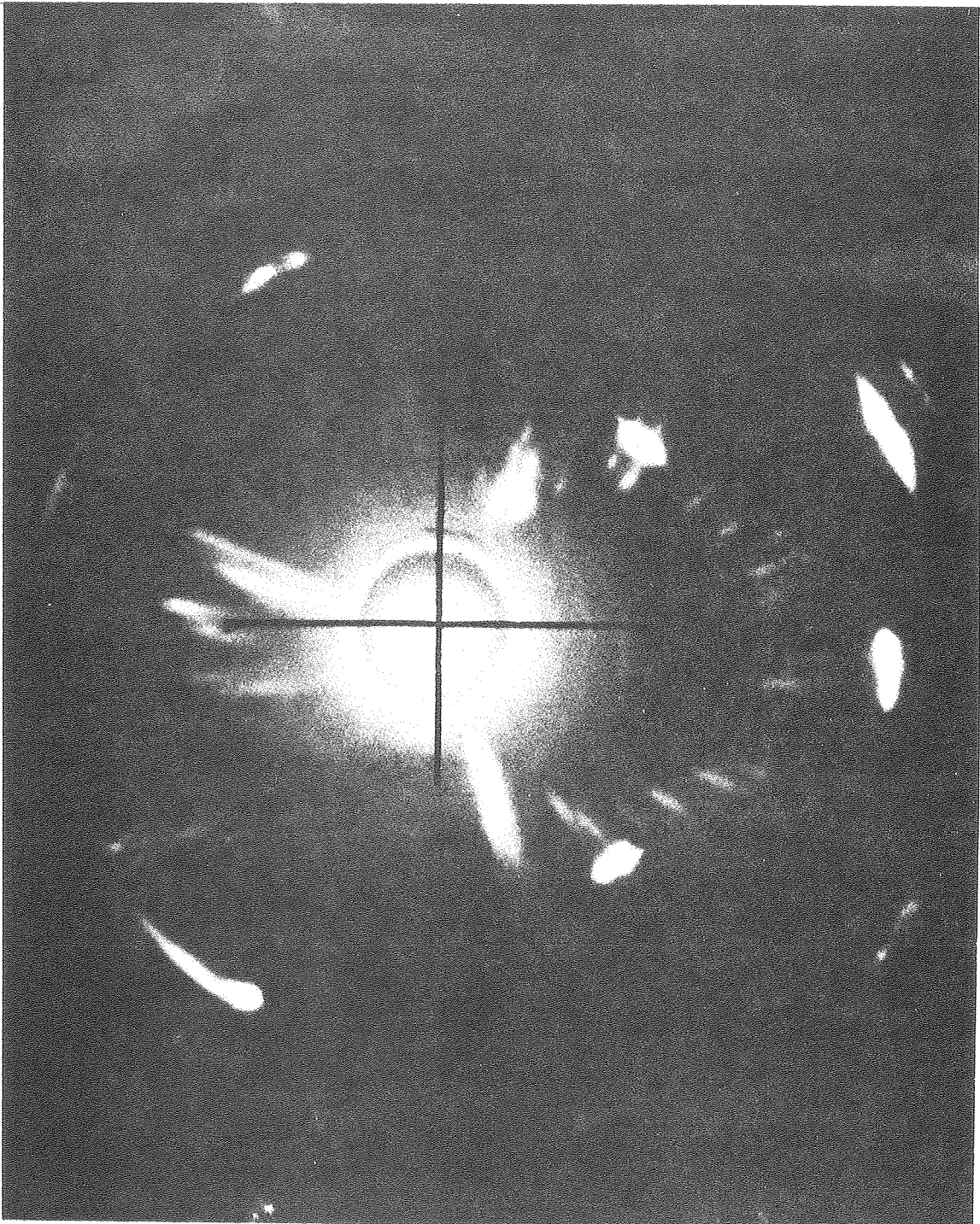
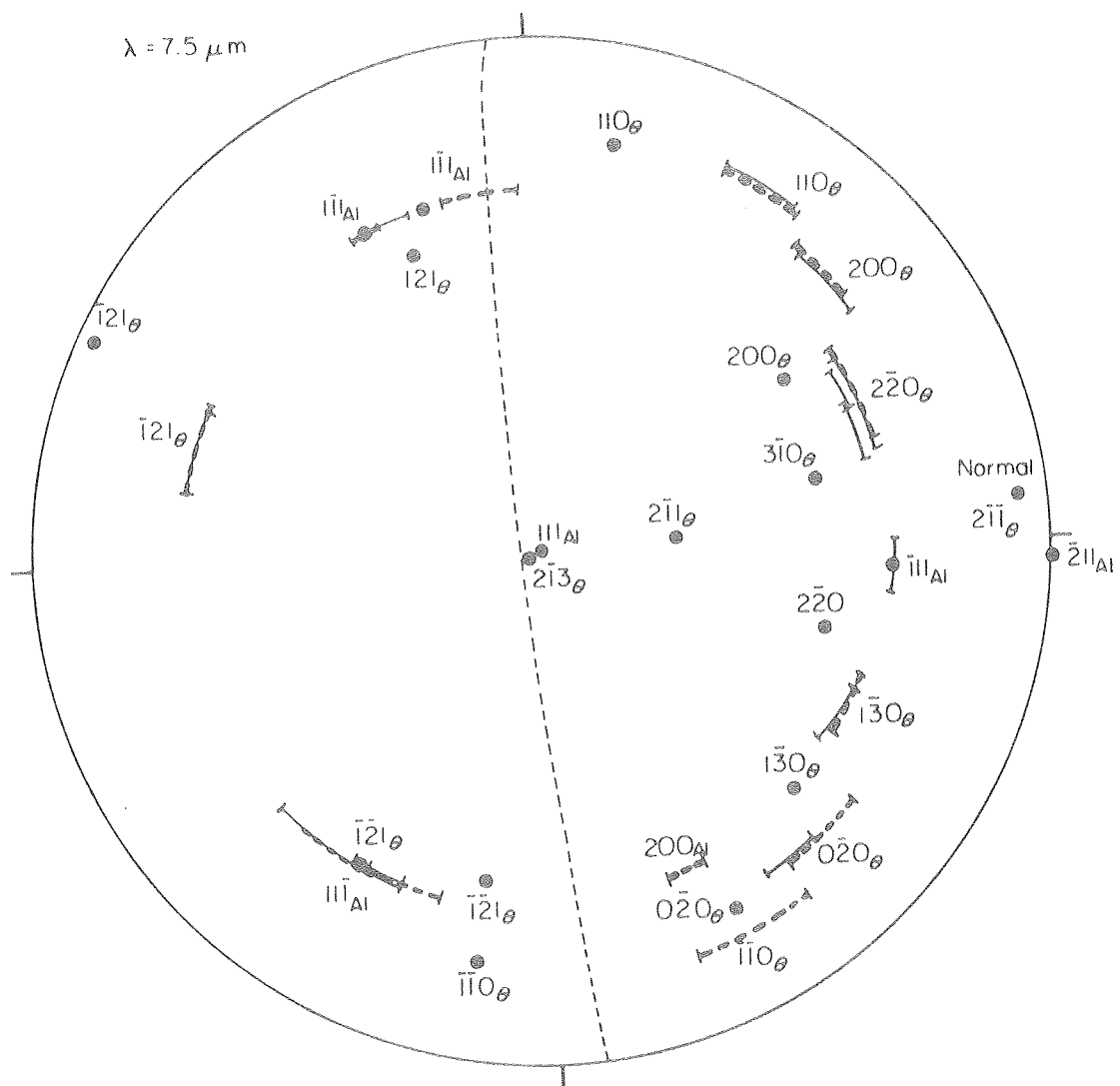


Figure 14



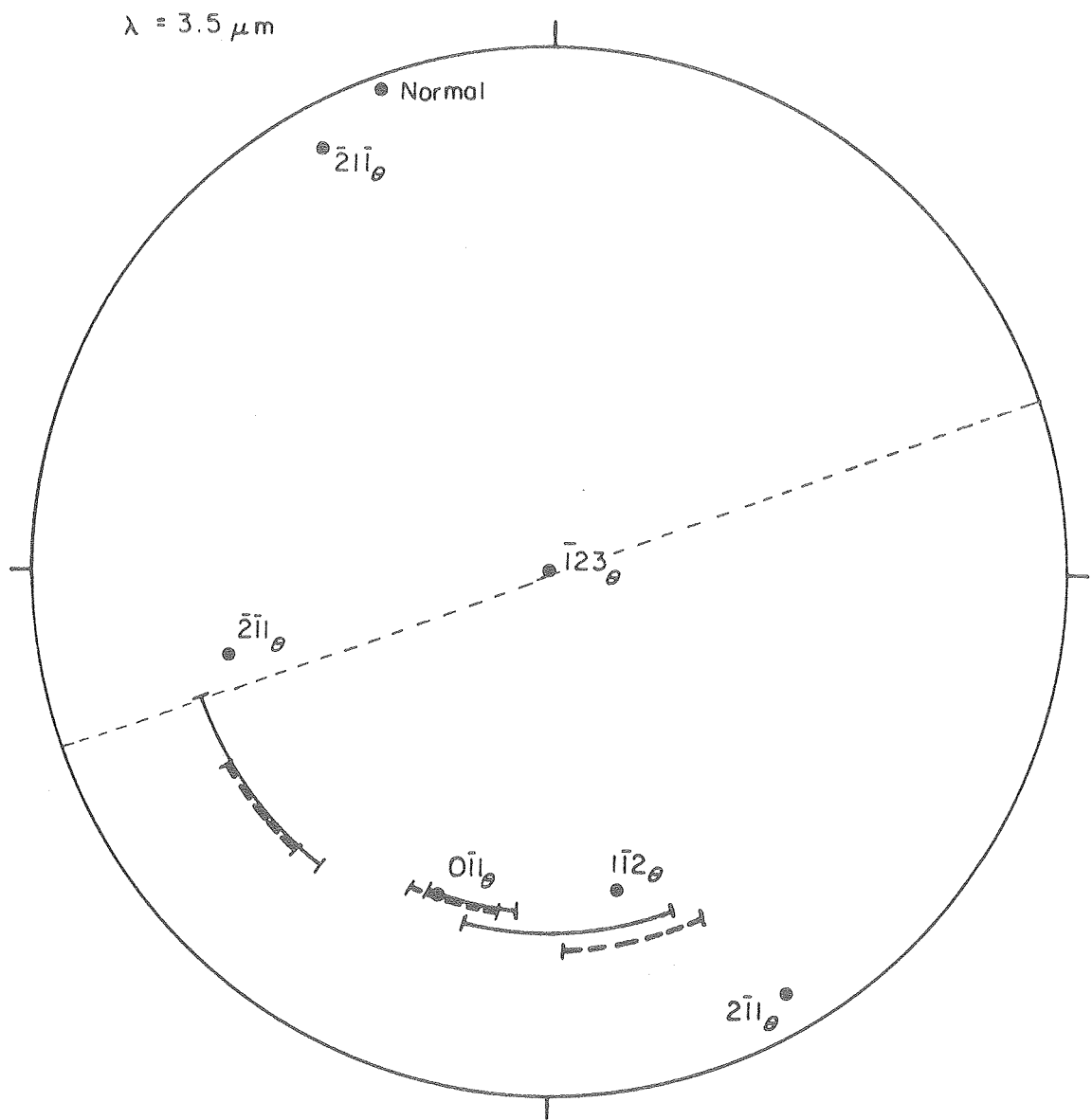
XBB 784-4429



XBL 783-4762

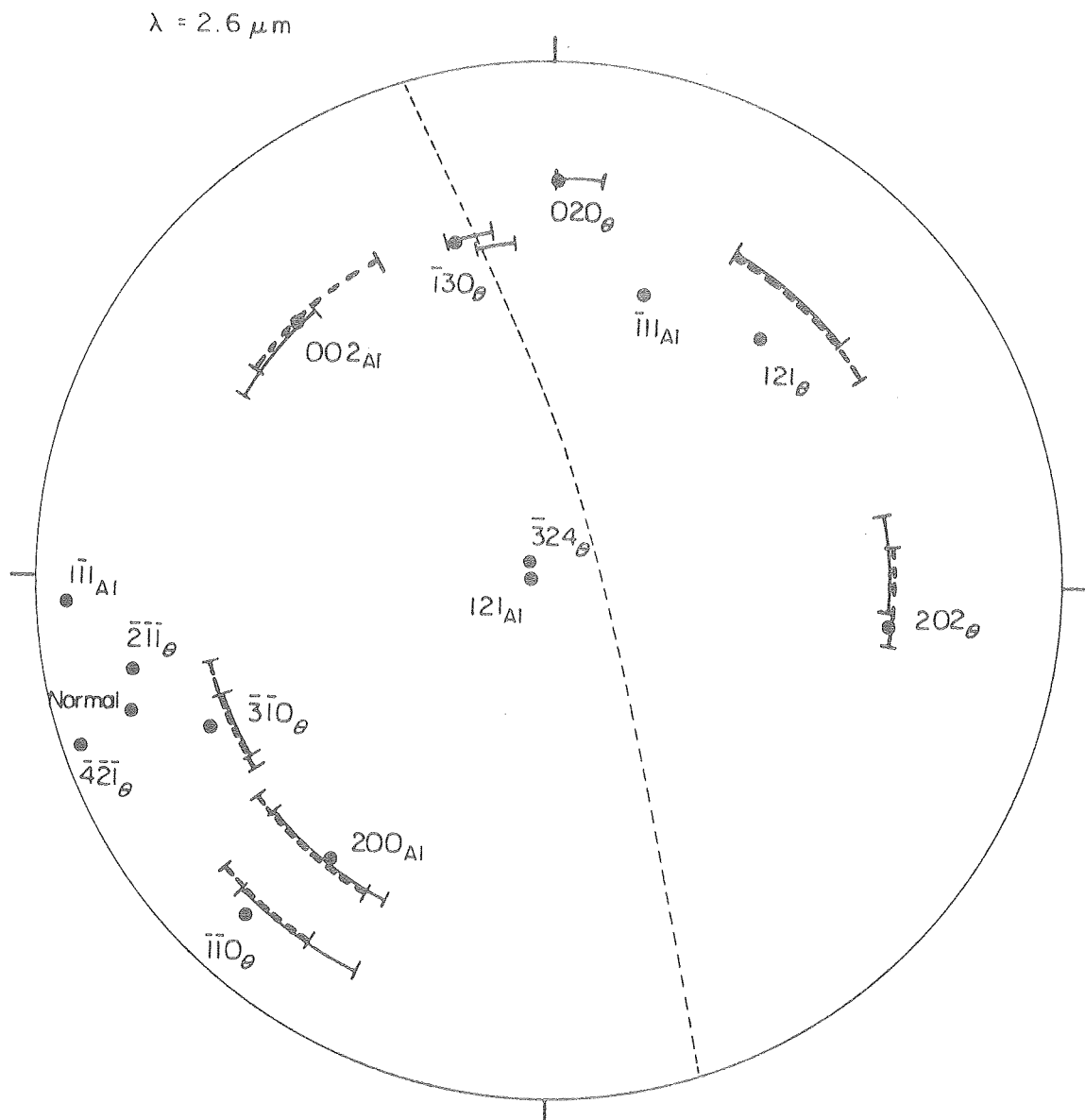
Figure 16





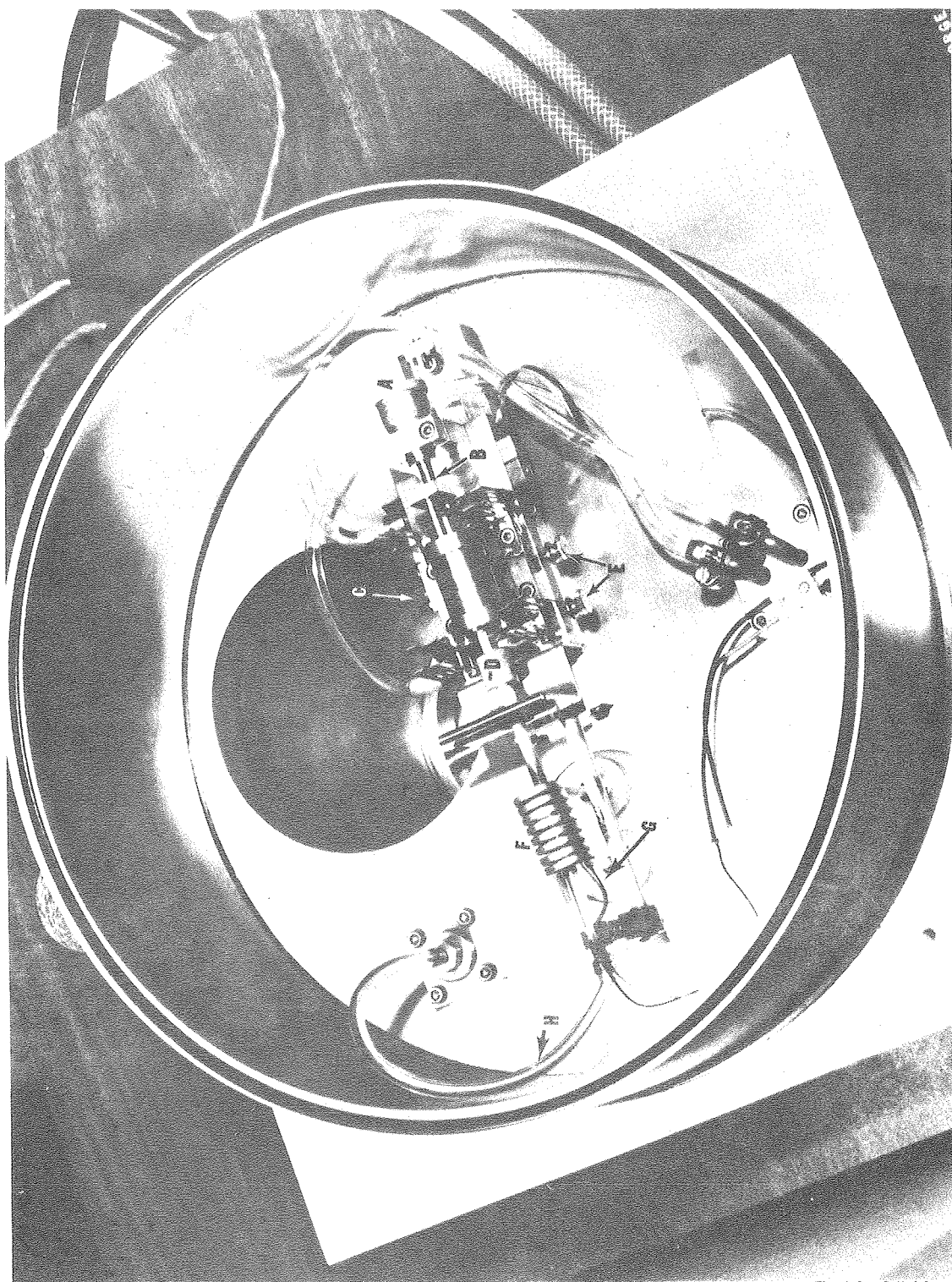
XBL 783-4764

Figure 17



XBL 783-4763

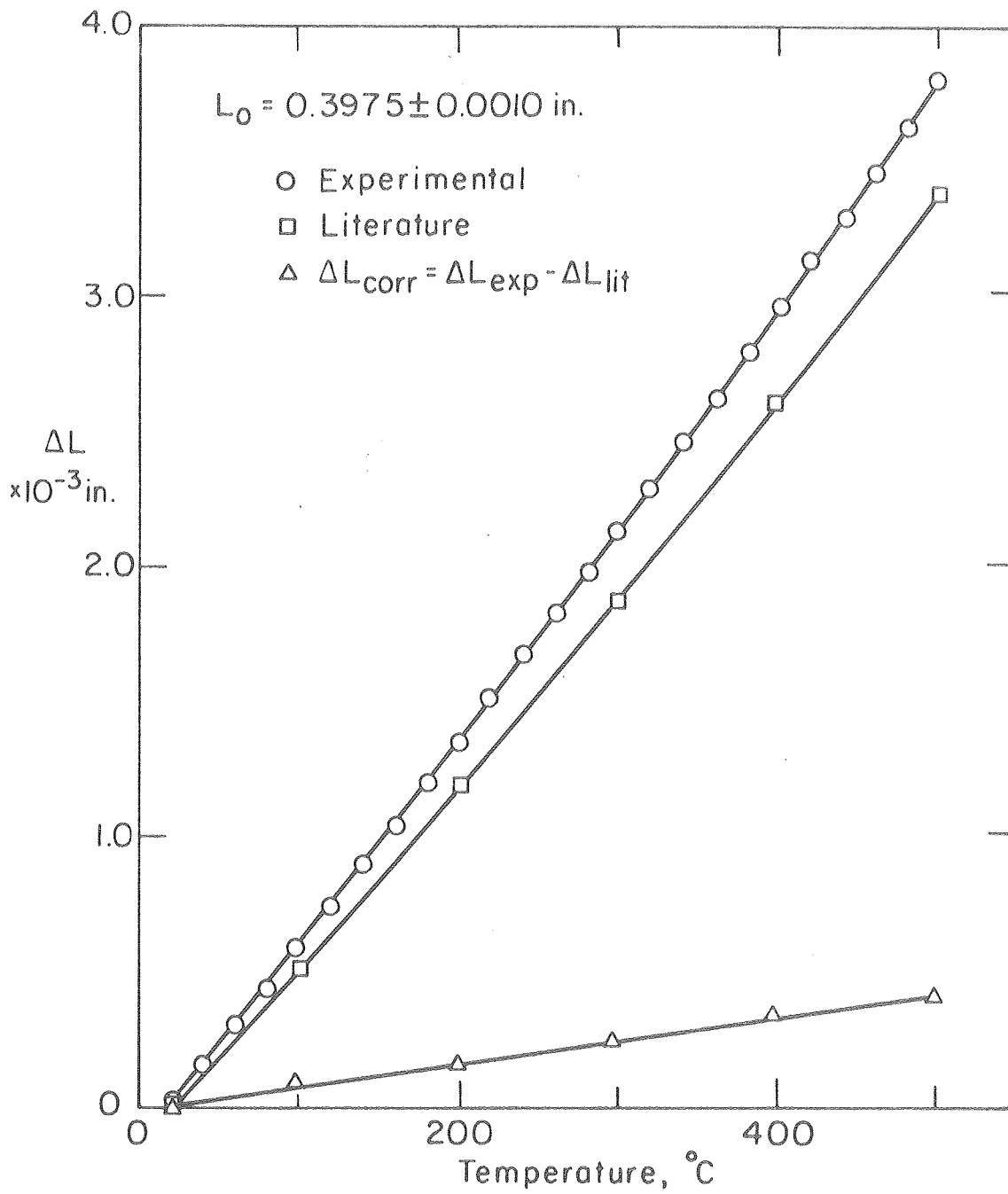
Figure 18



XBB 7512-2369B

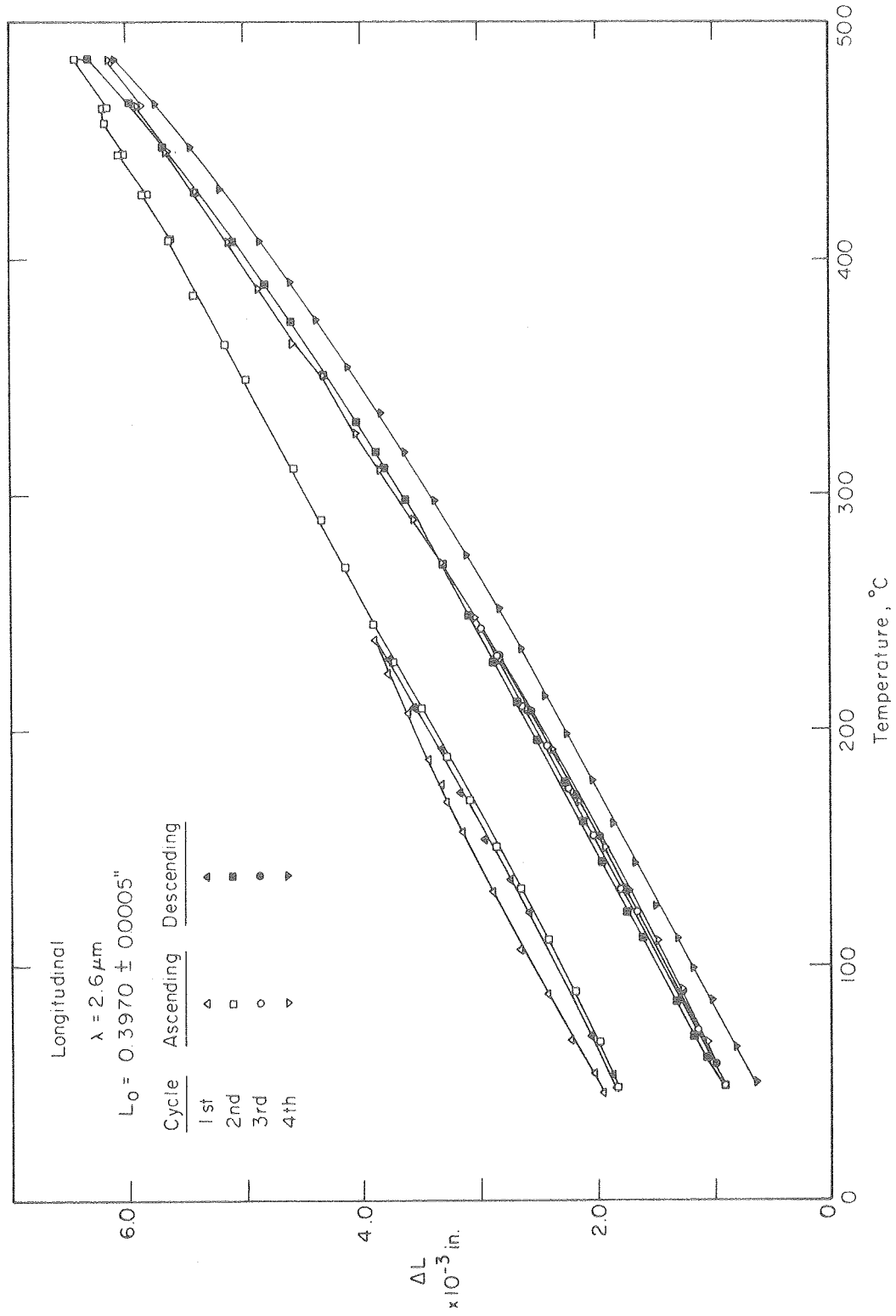
Figure 22





XBL7712-6621

Figure 24



XBL 782-4570

Figure 25

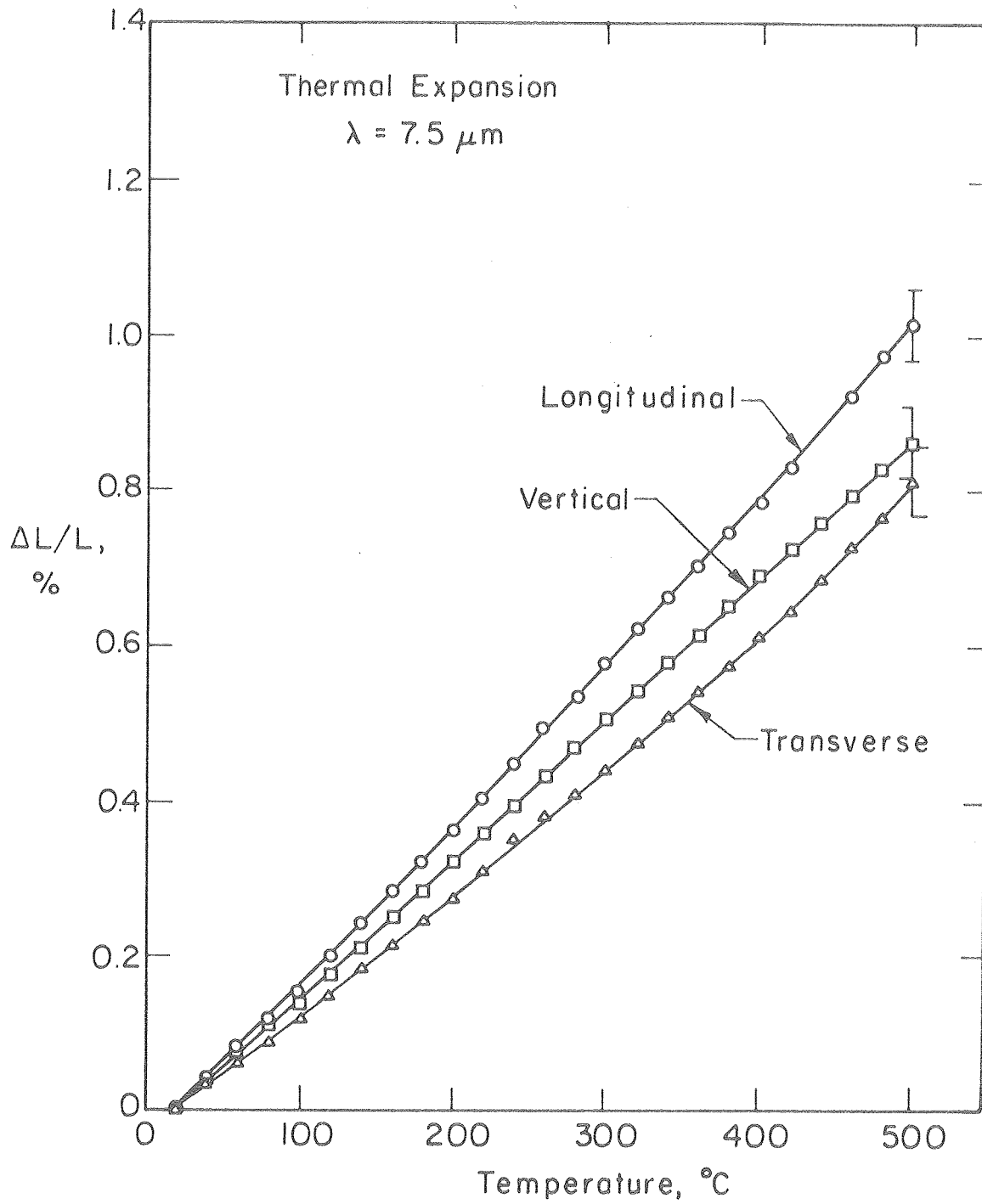


Figure 26

XBL 783 - 4773

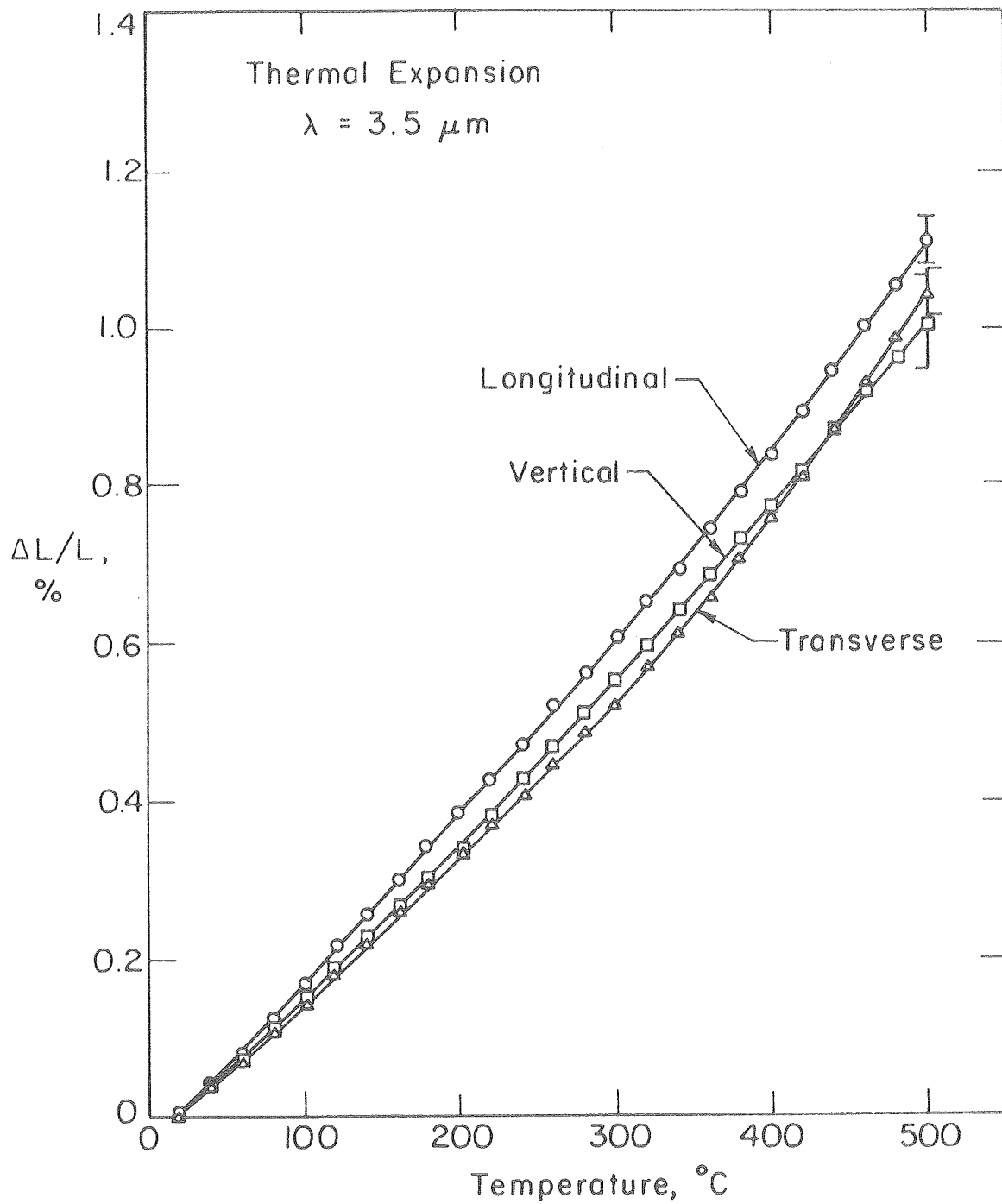


Figure 27

XBL 783-4774



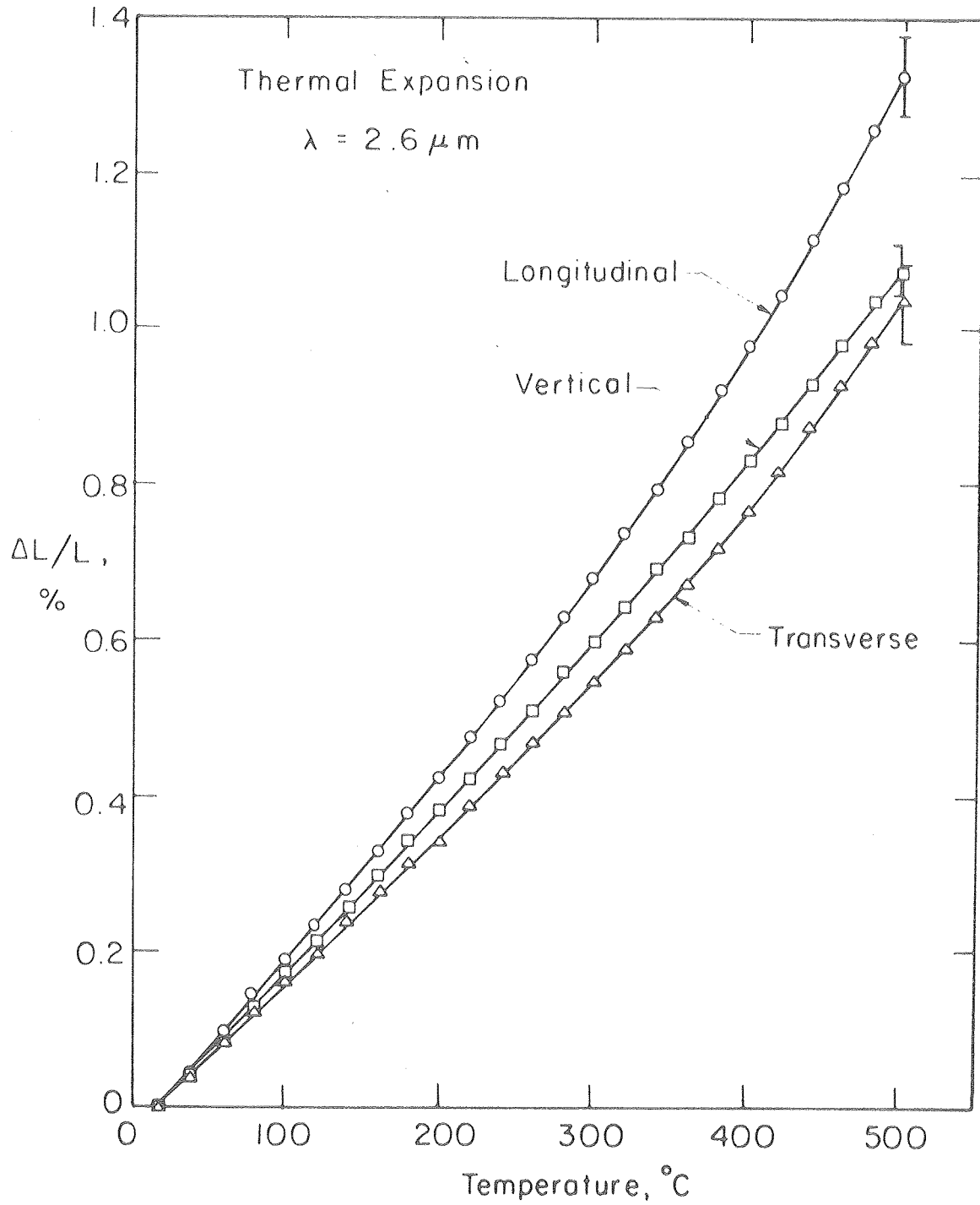
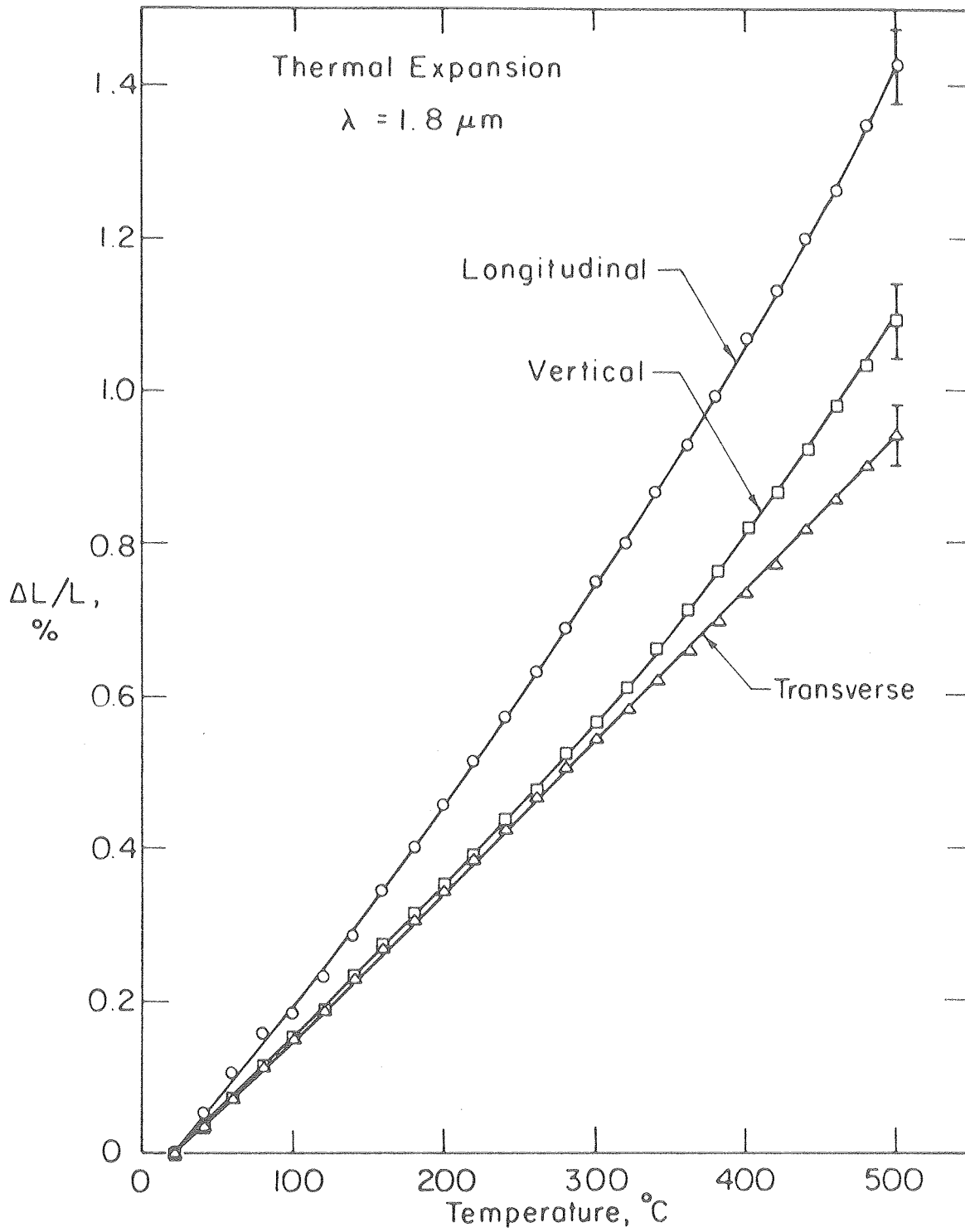


Figure 28

XBL 78 2 -4569



XBL782-4571

Figure 29

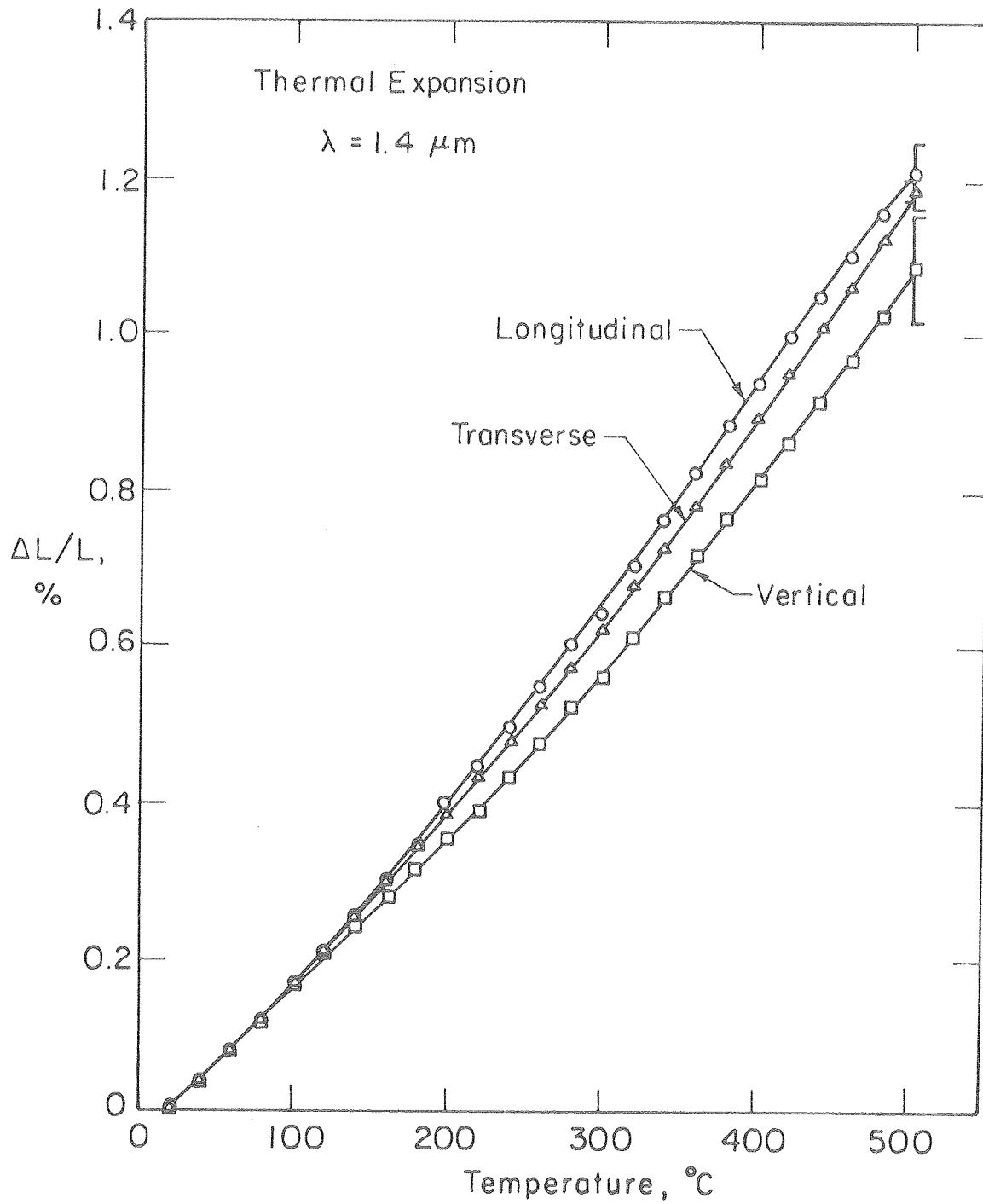


Figure 30

XBL 783-4772

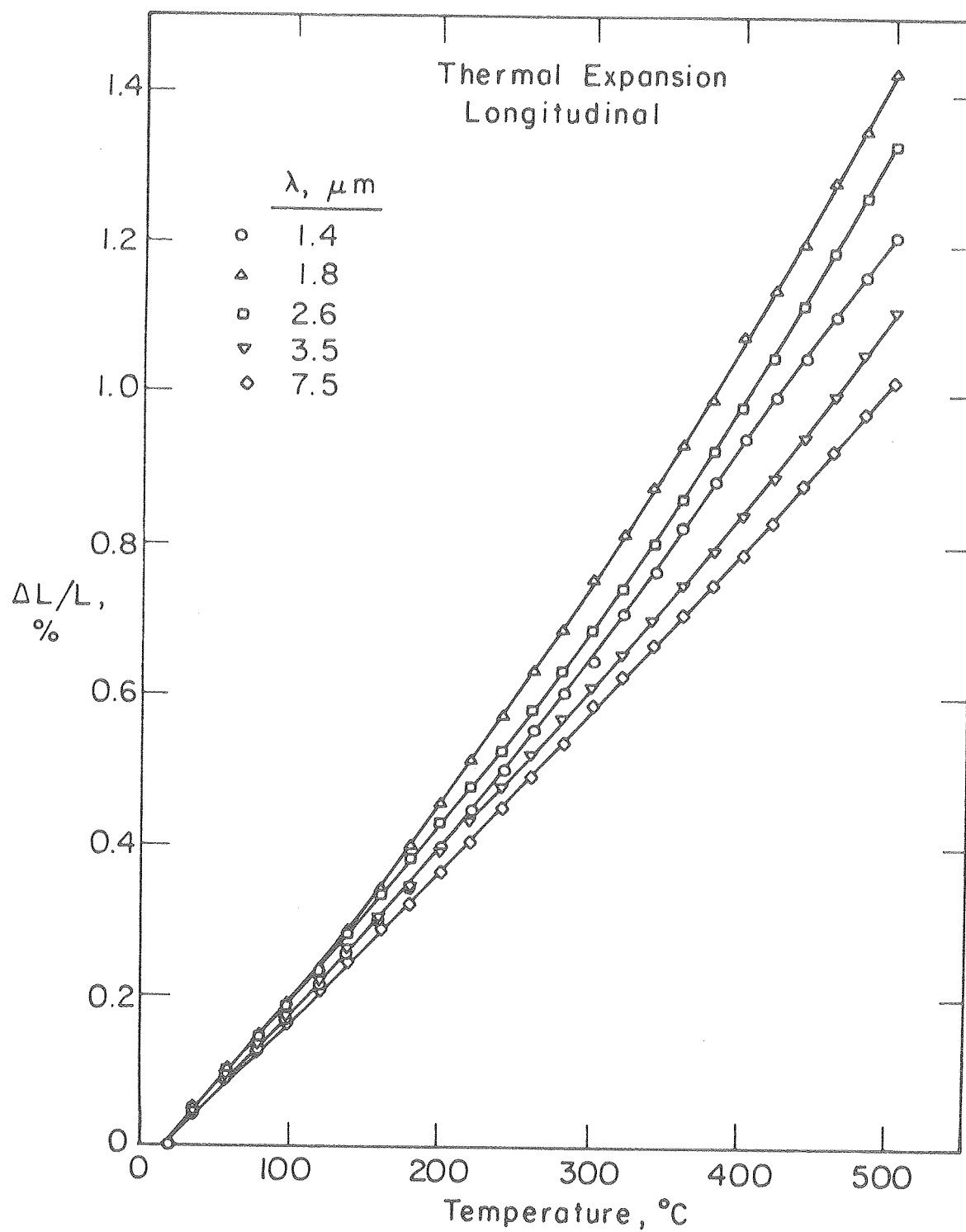


Figure 31

X BL 783-4777

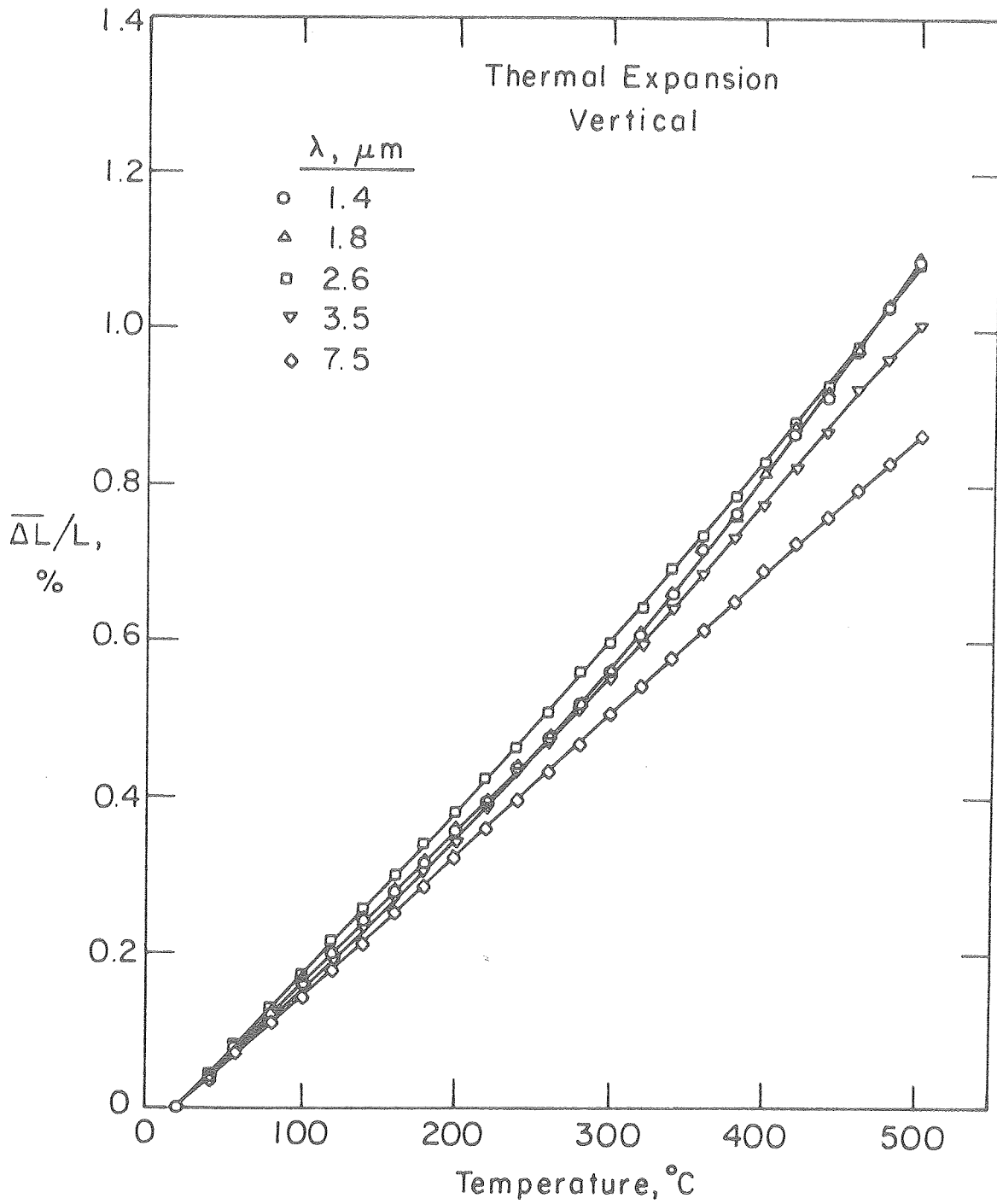


Figure 32

XBL 783- 4775

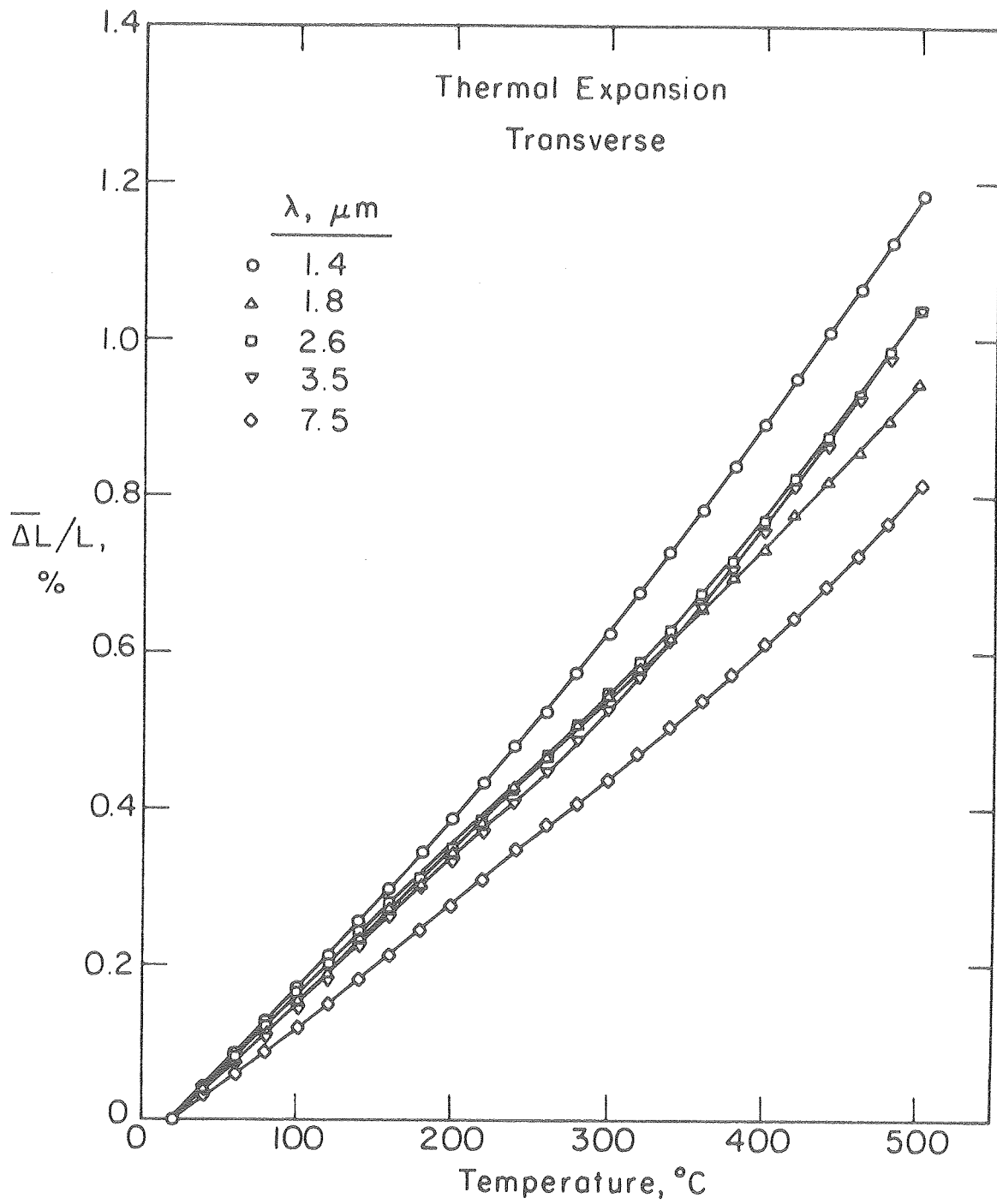


Figure 33

XBL783-4776

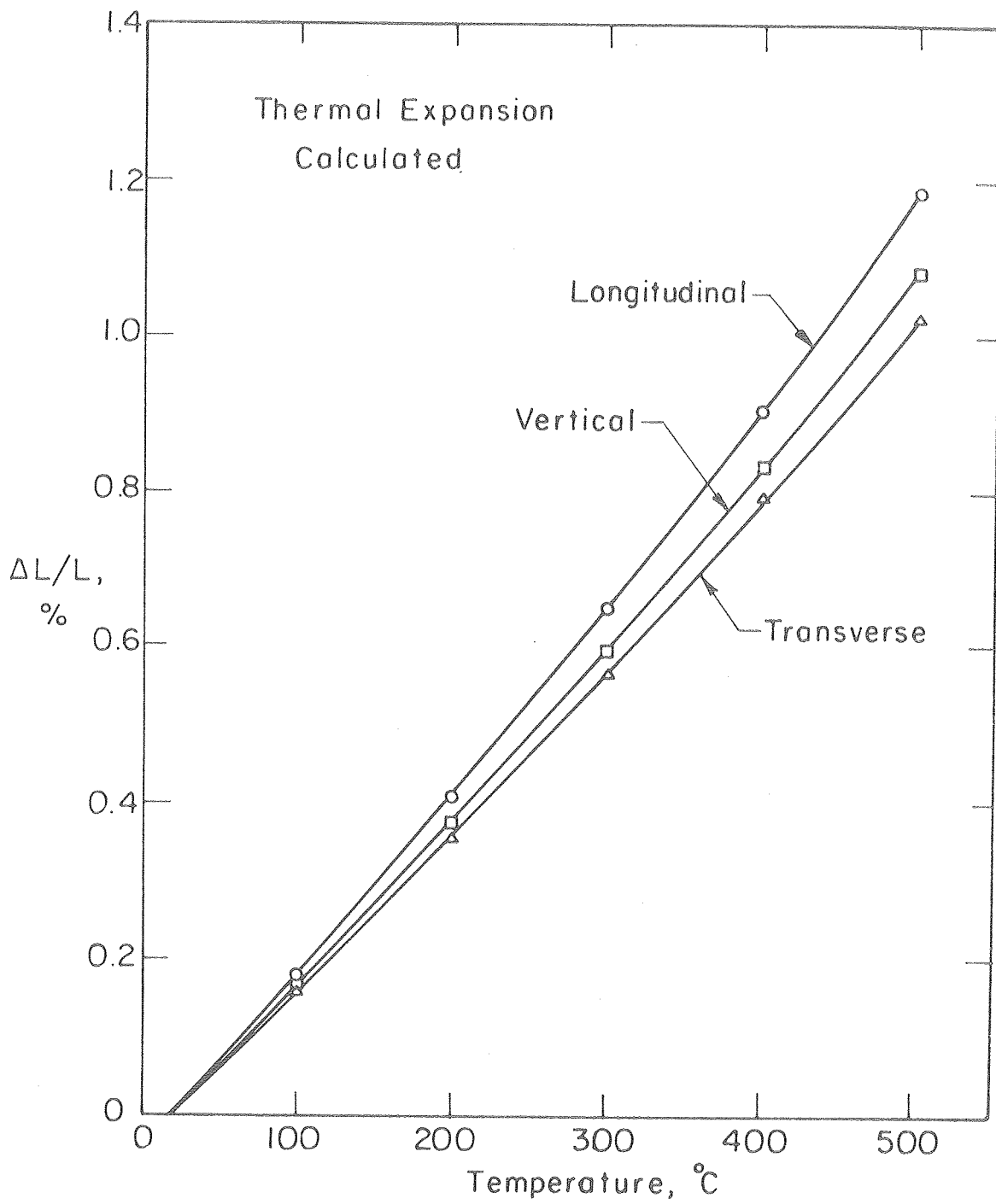


Figure 34

XBL 783-4771